



1 **Do surface lateral flows matter for data assimilation of soil moisture observations**

2 **into hyperresolution land models?**

3 **Running title: HYPERRESOLUTION LAND DATA ASSIMILATION**

4 Yohei Sawada<sup>1,2</sup>,

5 <sup>1</sup> Institute of Engineering Innovation, the University of Tokyo, Tokyo, Japan

6 <sup>2</sup> Meteorological Research Institute, Japan Meteorological Agency, Tsukuba, Japan

7

8

9 Corresponding author: Y. Sawada, Institute of Engineering Innovation, the University of

10 Tokyo, Tokyo, Japan, 2-11-6, Yayoi, Bunkyo-ku, Tokyo, Japan, [yohei.sawada@sogo.t.u-](mailto:yohei.sawada@sogo.t.u-)

11 [tokyo.ac.jp](http://tokyo.ac.jp)

12



13 **Abstract**

14 It is expected that hyperresolution land modeling substantially innovates the simulation  
15 of terrestrial water, energy, and carbon cycles. The major advantage of hyperresolution  
16 land models against conventional one-dimensional land surface models is that  
17 hyperresolution land models can explicitly simulate lateral water flows. Despite many  
18 efforts on data assimilation of hydrological observations into those hyperresolution land  
19 models, how and when surface water flows driven by local topography matter for data  
20 assimilation of soil moisture observations has not been fully clarified. Here I perform two  
21 minimalist synthetic experiments where soil moisture observations are assimilated into  
22 an integrated surface-groundwater land model by an ensemble Kalman filter. A horizontal  
23 background error covariance provided by overland flows is important to adjust the  
24 unobserved state and parameter variables. However, the non-Gaussianity of the  
25 background error provided by the nonlinearity of a topography-driven surface flow harms  
26 the performance of data assimilation. It is difficult to efficiently constrain model states at  
27 the edge of the area where the topography-driven surface flow reaches by linear-Gaussian  
28 filters, which brings the new challenge in land data assimilation for hyperresolution land  
29 models. This study highlights the importance of surface lateral flows in hydrological data  
30 assimilation.



31

32

### 33 **1. Introduction**

34 Hyperresolution land modeling is expected to improve the simulation of terrestrial water,  
35 energy, and carbon cycles, which is crucially important for meteorological, hydrological  
36 and ecological applications (see Wood et al. (2011) for a comprehensive review). While  
37 conventional land surface models (LSMs) assume that lateral water flows are negligible  
38 at the coarse resolution and solve vertical one-dimensional Richards equation for the soil  
39 moisture simulation (e.g., Sellers et al. 1996; Lawrence et al. 2011), currently proposed  
40 hyperresolution land models, which can be applied at a finer resolution (<1km), explicitly  
41 consider surface and subsurface lateral water flows (e.g., Maxwell and Miller 2005; Tian  
42 et al. 2012; Shrestha et al. 2014; Niu et al. 2014). The fine horizontal resolution can  
43 resolve slopes, which are drivers of a lateral transport of water, and realize the fully  
44 integrated surface-groundwater modeling. Previous works indicated that a lateral  
45 transport of water plays an important role in terrestrial water and energy cycles (e.g.,  
46 Maxwell and Condon 2016; Ji et al. 2017; Fang et al. 2017) and land-atmosphere  
47 interactions (e.g., Williams and Maxwell 2011; Keune et al. 2016).

48



49 Data assimilation has contributed to improving the performance of LSMs by fusing  
50 simulation and observation. The grand challenge of land data assimilation is to estimate  
51 unobservable variables from observations by propagating observations' information into  
52 model's high dimensional state and parameter space. In previous works on the  
53 conventional 1-D LSMs, many land data assimilation systems (LDASs) have been  
54 proposed to accurately estimate model's state and parameter variables, which cannot be  
55 directly observed, by assimilating satellite and in-situ observations. For example, the  
56 optimization of LSM's unknown parameters (e.g., hydraulic conductivity) has been  
57 implemented by assimilating remotely sensed microwave observations (e.g., Yang et al.  
58 2007; Yang et al. 2009; Bandara et al. 2014; Bandara et al. 2015; Sawada and Koike 2014;  
59 Han et al. 2014). Kumar et al. (2009) focused on the correlation between surface and root-  
60 zone soil moistures to examine the potential of assimilating surface soil moisture  
61 observations to estimate root-zone soil moisture. Sawada et al. (2015) successfully  
62 improved the simulation of root-zone soil moisture by the data assimilation of microwave  
63 brightness temperature observations which include the information of vegetation water  
64 content. Gravity Recovery and Climate Experiment total water storage observation has  
65 been intensively used to improve the simulation of groundwater and soil moisture (e.g.,  
66 Li et al. 2012; Houborg et al. 2012). Improving the simulation of state variables such as



67 soil moisture and biomass by LDASs has contributed to accurately estimating fluxes such  
68 as evapotranspiration (e.g. Martens et al. 2017) and CO<sub>2</sub> flux (e.g., Verbeeck et al. 2011).  
69 However, in most of the studies on the conventional 1-D LDASs, observations impacted  
70 state and parameter variables only in a single model's horizontal grid which is identical  
71 to the location of the observation. The assumption that the water flows are restricted to  
72 vertical direction in LSMs makes it difficult to propagate observation's information  
73 horizontally, which limits the potential of land data assimilation to fully use land  
74 hydrological observations.

75

76 The hyperresolution land models, which explicitly solve surface and subsurface lateral  
77 flows, provide a unique opportunity to examine the potential of land data assimilation to  
78 propagate observation's information horizontally in a model space and efficiently use land  
79 hydrological observations. Previous works successfully applied Ensemble Kalman Filters  
80 (EnKF) to 3-D Richards' equation-based integrated surface-groundwater models. For  
81 example, Camporese et al. (2009) and Camporese et al. (2010) successfully assimilated  
82 synthetic observations of surface pressure head and streamflow into the Catchment  
83 Hydrology (CATHY). Ridler et al. (2014) successfully assimilated Soil Moisture and  
84 Ocean Salinity satellite-observed surface soil moisture into the MIKE SHE distributed



85 hydrological model (see also Zhang et al. (2015)). Kurtz et al. (2016) coupled the Parallel  
86 Data Assimilation Framework (PDAF) (Nerger and Hiller 2013) with the Terrestrial  
87 System Modelling Framework (TerrSysMP) (Shrestha et al. 2014). The performance of  
88 TerrSysMP-PDAF to assimilate soil moisture observations was evaluated by a simple  
89 synthetic experiment (see also Zhang et al. (2018)). Those studies have significantly  
90 contributed to fully assimilating the new high-resolution soil moisture observations such  
91 as Sentinel-1 (e.g., Paroscia et al. 2013)

92

93 Although the data assimilation of hydrological observations into hyperresolution land  
94 models has been successfully implemented in the synthetic experiments, it is unclear how  
95 and when topography-driven surface lateral water flows matter for data assimilation of  
96 soil moisture observations. Previous studies on data assimilation with high resolution  
97 models mainly focused on assimilating groundwater observations (e.g., Ait-El-Fquih et  
98 al. 2016; Rasmussen et al. 2015; Hendricks-Franssen et al. 2008). There are some  
99 applications which focused on the observation of soil moisture and pressure head in  
100 shallow unsaturated soil layers. However, in those studies, topography-driven surface  
101 flow has not been considered in the experiment (Kurtz et al. 2016) or the role of them in  
102 assimilating observations into the hyperresolution land models has not been quantitatively



103 discussed (Camporese et al. 2010; Camporese et al. 2009). This study aims at clarifying  
104 if surface lateral flows matter for data assimilation of soil moisture observations into  
105 hyperresolution land models by a minimalist numerical experiment.

106

107

## 108 **2. Methods**

### 109 2.1. Model

110 ParFlow is an open source platform which realizes fully integrated surface-groundwater  
111 flow modeling (Kollet and Maxwell 2006; Maxwell et al. 2015). This parallel simulation  
112 platform has been widely used as a core hydrological module in hyperresolution land  
113 models (e.g., Maxwell and Kollet 2008; Maxwell and Condon 2016; Fang et al. 2017;  
114 Kurtz et al. 2016; Maxwell et al. 2011; Williams and Maxwell 2011; Shrestha et al. 2014).

115 A brief description on the method of ParFlow to simulate integrated surface-subsurface  
116 water flows can be found below and the complete description of ParFlow can be found in  
117 Kollet and Maxwell (2006), Maxwell et al. (2015) and references therein.

118

119 In the subsurface, ParFlow solves the variably saturated Richards equation in three  
120 dimensions.



121  $S_S S_W(h) \frac{\partial h}{\partial t} + \phi S_W(h) \frac{\partial S_W(h)}{\partial t} = \nabla \cdot \mathbf{q} + q_r$  (1)

122  $\mathbf{q} = -\mathbf{K}_s(\mathbf{x}) k_r(h) [\nabla(h+z) \cos\theta_x + \sin\theta_x]$  (2)

123 In equation (1),  $h$  is the pressure head [L];  $z$  is the elevation with the  $z$  axis specified as  
124 upward [L];  $S_S$  is the specific storage [ $L^{-1}$ ];  $S_W$  is the relative saturation;  $\phi$  is the  
125 porosity [-];  $q_r$  is a source/sink term. Equation (2) describes the flux  $\mathbf{q}$   
126 [ $LT^{-1}$ ] by Darcy's law, and  $\mathbf{K}_s$  is the saturated hydraulic conductivity tensor [ $LT^{-1}$ ];  $k_r$   
127 is the relative permeability [-];  $\theta$  is the local angle of topographic slope (see Maxwell et  
128 al. 2015). In this paper, the saturated hydraulic conductivity is assumed to be isotropic  
129 and a function of  $z$ :

130  $\mathbf{K}_s = K_s(z) = K_{s,surface} \exp(-f(z_{surface} - z))$  (3)

131 where  $K_{s,surface}$  is the saturated hydraulic conductivity at the surface soil, and  $z_{surface}$   
132 is the elevation of the soil surface. The saturated hydraulic conductivity decreases  
133 exponentially as the soil depth increases (Beven 1982). A van Genuchten relationship  
134 (van Genuchten 1980) is used for the relative saturation and permeability functions.

135

136 Overland flow is solved by the two-dimensional kinematic wave equation. The dynamics  
137 of the surface ponding depth,  $h$  [L], can be described by:

138  $\mathbf{k} \cdot [-K_s(z) k_r(h) \cdot \nabla(h+z)] = \frac{\partial \|h, 0\|}{\partial t} - \nabla \cdot \|h, 0\| \mathbf{v}_{sw} + q_r$  (4)





139 In equation (4),  $\mathbf{k}$  is the unit vector in the vertical and  $\|h, 0\|$  indicates the greater value  
140 of the two quantities following the notation of Maxwell et al. (2015). If  $h < 0$ , equation  
141 (4) describes that vertical fluxes across the land surface is equal to the source/sink term  
142  $q_r$  (i.e., rainfall and evapotranspiration). If  $h > 0$ , the terms on the right-hand side of  
143 equation (4), which indicate water fluxes routed according to surface topography, are  
144 active.  $\mathbf{v}_{sw}$  is the two-dimensional depth-averaged water flow velocity [ $\text{LT}^{-1}$ ] and  
145 estimated by the Manning's law:

$$146 \quad \mathbf{v}_{sw} = \left( \frac{\frac{\sqrt{S_{f,x}}}{n} h^{\frac{2}{3}}}{\frac{\sqrt{S_{f,y}}}{n} h^{\frac{2}{3}}} \right) \quad (5)$$

147 where  $S_{f,x}$  and  $S_{f,y}$  are the friction slopes [-] for the x- and y-direction, respectively;  $n$   
148 is the Manning's coefficient [ $\text{TL}^{-1/3}$ ]. In the kinematic wave approximation, the friction  
149 slopes are set to the bed slopes. The methodology of discretization and numerical method  
150 to solve equations (1-5) can be found in Kollet and Maxwell (2006).

151

152

## 153 2.2. Data Assimilation

154 In this paper, the ensemble Kalman filter (EnKF) was applied to assimilate soil moisture  
155 observations into ParFlow. The general description of the Kalman filter is the following:

$$156 \quad \mathbf{x}^f(t) = \mathcal{M}[\mathbf{x}^a(t-1)] \quad (6)$$



157  $\mathbf{x}^a(t) = \mathbf{x}^f(t) + \mathbf{K}[\mathbf{y}^o - \mathcal{H}\mathbf{x}^f(t)]$  (7)

158  $\mathbf{K} = \mathbf{P}^f \mathcal{H}^T (\mathcal{H} \mathbf{P}^f \mathcal{H}^T + \mathbf{R})^{-1}$  (8)

159  $\mathbf{P}^a = (\mathbf{I} - \mathbf{K} \mathcal{H}) \mathbf{P}^f$  (9)

160 I follow the notation of Houtekamer and Zhang (2016). In equation (6), a forecast model  
161  $\mathcal{M}$  (ParFlow in this study) is used to obtain a prior estimate at time  $t$ ,  $\mathbf{x}^f(t)$ , from the  
162 estimation at the previous time  $\mathbf{x}^a(t-1)$ . In equation (7), a prior estimate  $\mathbf{x}^f(t)$  is  
163 updated to the analysis state,  $\mathbf{x}^a(t)$ , using new observations  $\mathbf{y}^o$ . The Kalman gain matrix  
164  $\mathbf{K}$ , calculated by equation (8), gives an appropriate weight for the observations with an  
165 error covariance matrix  $\mathbf{R}$ , and the prior with an error covariance matrix  $\mathbf{P}^f$ . To calculate  
166  $\mathbf{K}$ , the observation operator  $\mathcal{H}$  is needed to map from model space to observation space.  
167 It should be noted that the equations (6-9) give an optimal estimation only when the model  
168 and observation errors follow the Gaussian distribution. When the probabilistic  
169 distribution of the error in either model or observation has a non-Gaussian structure,  
170 results of the Kalman filter are suboptimal. This point is important to interpret the results  
171 of this study.

172

173 EnKF is the Monte Carlo implementation of equations (6-9). To compute the Kalman gain  
174 matrix,  $\mathbf{K}$ , ensemble approximations of  $\mathbf{P}^f \mathcal{H}^T$  and  $\mathcal{H} \mathbf{P}^f \mathcal{H}^T$  can be given by:



175 
$$\mathbf{P}^f \mathbf{H}^T \equiv \frac{1}{k-1} \sum_{i=1}^k (\mathbf{x}_i^f - \bar{\mathbf{x}}^f) (\mathcal{H} \mathbf{x}_i^f - \overline{\mathcal{H} \mathbf{x}^f})^T \quad (10)$$

176 
$$\mathbf{H} \mathbf{P}^f \mathbf{H}^T \equiv \frac{1}{k-1} \sum_{i=1}^k (\mathcal{H} \mathbf{x}_i^f - \overline{\mathcal{H} \mathbf{x}^f}) (\mathcal{H} \mathbf{x}_i^f - \overline{\mathcal{H} \mathbf{x}^f})^T \quad (11)$$

177 where  $\mathbf{x}_i^f$  is the  $i$ th member of a  $k$ -member ensemble prior and  $\bar{\mathbf{x}}^f = \frac{1}{k} \sum_{i=1}^k \mathbf{x}_i^f$  and

178 
$$\overline{\mathcal{H} \mathbf{x}^f} = \frac{1}{k} \sum_{i=1}^k \mathcal{H} \mathbf{x}_i^f.$$

179

180 Once  $\bar{\mathbf{x}}^a = \sum_{i=1}^k \mathbf{x}_i^a$  ( $\mathbf{x}_i^a$  is the  $i$ th member of a  $k$ -member ensemble analysis) and  $\mathbf{P}^a =$

181  $\frac{1}{k-1} \sum_{i=1}^k (\mathbf{x}_i^a - \bar{\mathbf{x}}^a) (\mathbf{x}_i^a - \bar{\mathbf{x}}^a)^T$  are computed by equations (6-11), there are many

182 choices of an analysis ensemble. Although equations (6-11) can calculate the mean and

183 variance of the ensemble members, they do not tell how to adjust the state of the ensemble

184 members in order to realize the estimated mean and variance. There are many proposed

185 flavors of EnKF and one of the differences among them is the method to choose the

186 analysis  $\mathbf{x}_i^a$ . In this paper, the Ensemble Transform Kalman Filter (ETKF; Bishop et al.

187 2001; Hunt et al. 2007) was used to transport forecast ensembles to analysis ensembles.

188 Please refer to Hunt et al. (2007) for the complete description of the ETKF and its

189 localized version, the Local Ensemble Transform Kalman Filter (LETKF). The open

190 source available at <https://github.com/takemasa-miyoshi/letkf> was used in this study as

191 the ETKF code library.

192



193 In many ensemble Kalman filter systems, the ensemble spread tends to become  
194 underdispersive without any ensemble inflation methods (Houtekamer and Zhang, 2016).  
195 In this paper, the relaxation to prior perturbation method (RTPP) of Zhang et al. (2004)  
196 was used to maintain an appropriate ensemble spread. In the RTPP, the computed analysis  
197 perturbations are relaxed back to the forecast perturbations:

$$198 \mathbf{x}_{i,new}^a = (1 - \alpha)(\mathbf{x}_i^a - \overline{\mathbf{x}}^a) + \alpha(\mathbf{x}_i^f - \overline{\mathbf{x}}^f), \quad 0 \leq \alpha \leq 1 \quad (12)$$

199 where  $\alpha$  was set to 0.975 in this study.

200

201 In the data assimilation experiments, I adjusted pressure head by data assimilation so that  
202  $\mathbf{x}^f$  is pressure head. Since the surface saturated hydraulic conductivity was also adjusted,  
203  $\mathbf{x}^f$  includes log-transformed  $K_{s,surface}$ . Since I assimilated volumetric soil moisture  
204 observations ( $\mathbf{y}^o$  are observed volumetric soil moisture), the van Genuchten relationship  
205 works as an observation operator  $\mathcal{H}$  in order to transport the model estimated pressure  
206 head into the observable volumetric soil moisture in this study.

207

208

209 **2.3. Kullback-Leibler divergence**



210 To evaluate the non-Gaussianity of the background error sampled by an ensemble, I used  
211 the Kullback-Leibler divergence (KLD) (Kullback and Leibler 1951):

$$212 \quad D_{KL}(p, q) = \sum_i p(i) \log \frac{p(i)}{q(i)} \quad (13)$$

213 where  $D_{KL}(p, q)$  is the KLD between two probabilistic distribution functions (PDFs),  $p$   
214 and  $q$ . If two PDFs are equal for all  $i$ ,  $D_{KL}(p, q) = 0$ . A large value for  $D_{KL}(p, q)$   
215 indicates that the two PDFs,  $p$  and  $q$ , substantially differ from each other. Therefore,  
216 the KLD can be used as an index to evaluate the closeness of two PDFs. It should be  
217 noted that the KLD is not symmetric ( $D_{KL}(p, q) \neq D_{KL}(q, p)$ ).

218

219

### 220 **3. Synthetic experiments**

#### 221 **3.1. Simple 2-D slope with homogeneous hydraulic conductivity**

##### 222 **3.1.1. Experiment Design**

223 The synthetic experiment was implemented to examine how topography-driven surface  
224 lateral flows contribute to efficiently propagating observation's information horizontally  
225 in the data assimilation of soil moisture observation. Two synthetic reference runs were  
226 created by Parflow. The 2-D domain has a horizontal extension of 4000m and a vertical  
227 extension of 5m. The domain of the virtual slope was horizontally discretized into 40 grid



228 cells with a size of 100m and vertically discretized into 50 grid cells with a size of 0.10m.  
229 The domain has a 25% slope. In two synthetic reference runs, it heavily rains only in the  
230 upper half of the slope ( $2000\text{m} < x < 4000\text{m}$ ). A constant rainfall rate of 50mm/h was  
231 applied for 3 hours and then the period with no rainfall and evaporation of 0.075mm/h  
232 lasted for 117 hours. This 120-hour rain/no rain cycle was repeatedly applied to the  
233 domain. There is no rainfall in the lower half of the slope ( $0\text{m} < x < 2000\text{m}$ ). The  
234 configurations described above were schematically shown in Figure 1a. The parameters  
235 of the van Genuchten relationship, alpha and n, were set to  $1.5 [\text{m}^{-1}]$  and 1.75, respectively.  
236 The porosity,  $\phi$  in equation (1), was set to 0.40. The Manning's coefficient, n in equation  
237 (5), was set to  $5.52 \times 10^{-6} [\text{m}^{-1/3}\text{h}]$ . These clayey soil properties described above are  
238 applied to the whole domain. The groundwater table was located at  $z=3\text{m}$  and the  
239 hydrostatic pressure gradient was assumed for the initial pressure heads in the unsaturated  
240 soil layers.  
241  
242 The difference between two synthetic reference runs is the value of saturated hydraulic  
243 conductivity. The surface saturated hydraulic conductivity,  $K_{s,surface}$  in equation (3),  
244 was set to 0.005 [m/h] in one reference, and 0.02 [m/h] in the other. These surface  
245 saturated hydraulic conductivities described above are applied to the whole domain.



246 Figure 1 shows the difference of the response to heavy rainfall between the two synthetic  
247 reference runs. In the case of the low saturated hydraulic conductivity (hereafter called  
248 the LOW\_K reference), larger surface lateral flows are generated than the case of the high  
249 saturated hydraulic conductivity (hereafter called the HIGH\_K reference). In the LOW\_K  
250 reference, the topography-driven surface lateral flows reach the left edge of the domain  
251 (Figure 1b). In the HIGH\_K reference, supplied water moves vertically rather than  
252 horizontally and the topography-driven surface flow reaches around  $x = 1000\text{--}1500\text{m}$   
253 (Figure 1d).

254

255 For the data assimilation experiment, an ensemble of 50 realizations was generated. Each  
256 ensemble member has different saturated hydraulic conductivity and rainfall rate.  
257 Lognormal multiplicative noise was added to surface saturated hydraulic conductivity  
258 and rainfall rate of the synthetic reference runs. This specification of uncertainty in  
259 rainfall was also adopted in Crow et al. (2011). The two parameters of the lognormal  
260 distribution, commonly called  $\mu$  and  $\sigma$ , were set to 0 and 0.15, respectively. The initial  
261 groundwater depth of each ensemble member was drawn from the uniform distribution  
262 from 2.0m to 3.5m. The hydrostatic pressure gradient was assumed for the initial pressure  
263 heads in the unsaturated soil layers.



264

265 The virtual hourly observations were generated by adding the Gaussian white noise whose  
266 mean is zero to the volumetric soil moisture simulated by the synthetic reference runs.

267 The observation error (the standard deviation of the added Gaussian white noise) was set  
268 to  $0.05 \text{ m}^3/\text{m}^3$ . It was assumed that the volumetric soil moistures can be observed in every

269 model's soil layer from surface to the depth of 1m at the specific location. The two  
270 scenarios of the observation's location are provided. In the first scenario (hereafter called

271 the UP\_O scenario), the volumetric soil moisture at the upper part of the slope ( $x =$   
272 2500m) was observed. In the UP\_O scenario, I could observe the volumetric soil moisture

273 in the upper part of the slope where it heavily rains and tried to infer the soil moisture in  
274 the lower part of the slope where it does not rain by propagating the observation's

275 information downhill. In the second scenario (hereafter called the DOWN\_O scenario),  
276 the volumetric soil moisture at the lower part of the slope ( $x = 1500\text{m}$ ) was observed. In

277 the DOWN\_O scenario, I could observe the volumetric soil moisture in the lower part of  
278 the slope where it does not rain and tried to infer the soil moisture in the upper part of the

279 slope where it heavily rains by propagating the observation's information uphill.

280





281 Since I had the two synthetic reference runs (the HIGH\_K and LOW\_K references) and  
282 the two observation scenarios (the UP\_O and DOWN\_O scenarios), I implemented totally  
283 four data assimilation experiments. Table 1 summarizes the data assimilation experiments  
284 implemented in this study. For instance, in the HIGH\_K-UP\_O experiment, I chose the  
285 HIGH\_K reference and generated an ensemble of 50 realizations from the HIGH\_K  
286 reference. The soil moisture observations were generated from the HIGH\_K reference at  
287 the location of  $x = 2500\text{m}$  and assimilated into the model every hour. The simulated  
288 volumetric soil moisture of the data assimilation experiment was compared with that of  
289 the HIGH\_K reference.

290

291 In addition to the data assimilation (DA) experiments, I implemented the NoDA  
292 experiment (also called the open-loop experiment in the literature of the LDAS study) in  
293 which the ensemble was used but no observation data were assimilated. As evaluation  
294 metrics, root-mean-square-error (RMSE) was used:

295 
$$\text{RMSE} = \sqrt{\frac{1}{k} \sum_{i=1}^k (F_i - T)^2} \quad (14)$$

296 where  $k$  is the ensemble number,  $F_i$  is the volumetric soil moisture simulated by the  $i$ -th  
297 member in the DA or NoDA experiment,  $T$  is the volumetric soil moisture simulated by  
298 the synthetic reference run.



299

300 To evaluate the impact of data assimilation, the improvement rate (IR) was defined and  
301 calculated by the following equation:

$$302 \quad IR = \frac{\overline{RMSE}_{DA} - \overline{RMSE}_{NoDA}}{\overline{RMSE}_{NoDA}} \quad (15)$$

303 where  $\overline{RMSE}_{DA}$  and  $\overline{RMSE}_{NoDA}$  are time-mean RMSE of the DA and NoDA  
304 experiments, respectively. The negative IR indicates that data assimilation positively  
305 impacts the simulation of soil moisture. The metrics described above was calculated in  
306 the whole domain. In the DA experiment, soil moisture values before the update by ETKF  
307 (i.e. initial guess) were used to calculate the metrics.

308

309 Four of 120-hour rain/no rain cycles were applied so that the computation period was 480  
310 hours. The spin-up results in the first 120 hours were not used to calculate the evaluation  
311 metrics. Since the steady state of groundwater level is not the scope of this paper, the long  
312 spin-up is not absolutely necessary.

313

314

315 **3.1.2. Results**



316 Figure 2a shows the IR of the LOW\_K-UP\_O experiment. The time series of the DA and  
317 NoDA experiment and the synthetic reference run in the LOW\_K-UP\_O experiment can  
318 be found in Figure S1. The data assimilation efficiently propagates the information of the  
319 observations located in the upper part of the slope (see the black arrow in Figure 2a) both  
320 horizontally and vertically. RMSE is reduced by data assimilation not only directly under  
321 the observation but also the lower part of the slope where it does not rain. The optimized  
322  $K_{s,surface} \approx 0.00508$  [m/h] is also accurate. However, the increase of RMSE by data  
323 assimilation can be found at the left edge of the domain, which is far from the location of  
324 the observation. The impact of data assimilation on the surface soil moisture simulation  
325 is small because the RMSE of the NoDA experiment is already small ( $\leq 0.01\text{m}^3/\text{m}^3$ ) there  
326 in the case of the LOW\_K reference so that any improvements there do not make sense.  
327

328 Figure 2b shows the IR of the LOW\_K-DOWN\_O experiment (see also Figure S2 for  
329 time series). The IR's spatial pattern of the LOW\_K-DOWN\_O experiment is similar to  
330 that of the LOW\_K-UP\_O experiment. It is promising that I can accurately infer soil  
331 moisture in the region where it heavily rains from the shallow soil moisture observations  
332 in the region where it does not rain. The optimized  $K_{s,surface} \approx 0.00512$  [m/h] is also  
333 accurate.



334

335 Figure 3a shows the difference of time-mean RMSEs ( $\overline{RMSE}_{DA}$  in equation (15))  
336 between the LOW\_K-UP\_O and LOW\_K-DOWN\_O experiments. Although observing  
337 the lower part of the slope slightly improves the soil moisture simulation at the left edge  
338 of the domain compared with observing the upper part of the slope, there are few  
339 differences between the UP\_O and DOWN\_O scenarios in the case of the LOW\_K  
340 reference. The soil moisture observations have large representativeness and I can  
341 efficiently infer soil moisture in the soil columns which are horizontally and vertically far  
342 from the observations.

343

344 Figure 2c shows the IR of the HIGH\_K-UP\_O experiment (see also Figure S3 for time  
345 series). The data assimilation significantly reduces RMSE of the soil moisture simulation  
346 directly under the observations (see the black arrow in Figure 2c), which indicates that  
347 the data assimilation efficiently propagates the information of the observations vertically.  
348 The saturated hydraulic conductivity is also accurately optimized ( $K_{s,surface} \approx 0.0204$   
349 [m/h]). However, the impact of the data assimilation on the soil moisture simulation in the  
350 lower part of the slope around  $x=1500\text{m}$  is marginal although there are large RMSE in



351 the NoDA experiment ( $>0.05\text{m}^3/\text{m}^3$ ) at the edge of the area where topography-driven  
352 surface flow reaches in the HIGH\_K reference (see Figure 1d).

353

354 Figure 2d shows the IR of the HIGH\_K-DOWN\_O experiment (see also Figure S4 for  
355 time series). Although the observations in the lower part of the slope (see the black arrow

356 in Figure 2d) significantly improve the soil moisture simulation in the downstream area

357 of the observation and accurately optimize  $K_{s,surface} \approx 0.0208$  [m/h], the impact of the

358 data assimilation on the shallow soil moisture simulation around  $x=500\sim 1000\text{m}$  is

359 marginal. As I found in the LOW\_K-DOWN\_O experiment, the shallow soil moisture

360 observations in the region where it does not rain can improve the soil moisture simulation

361 in the region where it heavily rains. However, the IR of the HIGH\_K-DOWN\_O

362 experiment in the upper part of the slope is smaller than that of the LOW\_K-DOWN\_O

363 experiment (see Figure 2b and 2d).

364

365 The high representativeness of the observations which I found in the case of the LOW\_K

366 reference cannot be found in the case of the HIGH\_K reference. Figure 3b shows the

367 difference of time-mean RMSEs ( $\overline{RMSE_{DA}}$  in equation (15)) between the HIGH\_K-

368 UP\_O and HIGH\_K-DOWN\_O experiments. Compared with the LOW\_K reference case



369 (Figure 3a), there are significant differences between the UP\_O and DOWN\_O scenarios  
370 in the case of higher saturated hydraulic conductivity. In this case, the vertical propagation  
371 of the observations' information is more efficient than the horizontal propagation.

372

373 The relatively low efficiency of the data assimilation and the low representativeness of  
374 the soil moisture observations in the case of the HIGH\_K reference are caused by the  
375 non-Gaussian background error distribution. I calculated KLD by comparing the PDF of  
376 the NoDA ensemble ( $p$  in equation (13)) with the Gaussian PDF which has the mean and  
377 variance of the NoDA ensemble ( $q$  in equation (13)). Figure 4 shows that the NoDA  
378 ensemble in the case of the HIGH\_K reference has stronger non-Gaussianity than the case  
379 of the LOW\_K reference especially in the shallow soil layers. The strong non-Gaussianity  
380 of the NoDA ensemble generated from the HIGH\_K reference can be found at the edge  
381 of the area where the topography-driven surface flow reaches (Figure 1d). Figure 5 shows  
382 that there is the bifurcation of the ensemble in this region when the ensemble is generated  
383 from the HIGH\_K reference. The process of topography-driven surface flows is switched  
384 on if and only if the surface soil is saturated (see equation (4)) so that the ensemble tends  
385 to be bifurcated into the members with surface flows and without surface flows. As I  
386 mentioned in section 2.2, in the ETKF, the state and parameter variables are adjusted



387 assuming the Gaussian PDF of the model's error and the linear relationship between  
388 observed variables and unobserved variables. Therefore, the non-Gaussianity of the prior  
389 ensemble induced by the strong non-linear dynamics of surface lateral flows makes the  
390 ETKF inefficient. It is more difficult to reconstruct 3-D fields of soil moisture in high  
391 conductivity soils since the 1-D vertical water movement is more dominant. The absolute  
392 RMSE of the NoDA experiment in the HIGH\_K reference is larger than the LOW\_K  
393 reference in many places (not shown). Please note that the non-Gaussianity can also be  
394 found in the LOW\_K reference at the edge of the domain ( $x=500\text{m}$ ) due to the non-linear  
395 dynamics, which causes the degradation of the soil moisture simulation in the LOW\_K-  
396 UP\_O experiment (see Figure 2a).

397

398 One of the major simplifications in this experiment is spatially homogeneous surface  
399 saturated hydraulic conductivity. The optimization of it can efficiently improve the soil  
400 moisture simulation in the whole domain. However, the optimization of this  
401 homogeneous surface saturated hydraulic conductivity has a limited impact on the soil  
402 moisture simulation. Figure S5 shows the IR of the HIGH\_K-DOWN\_O experiment  
403 where the parameter optimization by ETKF is switched off. Even if I do not optimize the  
404 surface saturated hydraulic conductivity, I could obtain the similar IR to the original



405 experiment and the shallow soil moisture observations in the region where it does not rain  
406 can improve the soil moisture simulation in the region where it heavily rains. The  
407 horizontal propagation of the observations' information shown in this experiment was  
408 brought out not only by the optimization of spatially homogeneous saturated hydraulic  
409 conductivity but also by the horizontal error correlation due to topography-driven surface  
410 flows.

411

412 Please note that the improvement of the soil moisture simulation cannot be found if the  
413 topography-driven surface flow is neglected. Figure S6 shows the IR of the LOW-  
414 K\_DOWN-O experiment where the topography-driven surface flow is neglected in the  
415 ParFlow simulation. The imperfect model physics of ParFlow substantially degrades the  
416 skill to simulate soil moisture and data assimilation cannot compensate this degradation.  
417 This point will also be discussed in the section 3.2 more deeply.

418

## 419 **3.2. Simple 3-D slope with heterogeneous hydraulic conductivity**

### 420 **3.2.1. Experiment design**

421 To further demonstrate how land data assimilation works with topography-driven surface  
422 lateral flows, I implemented another synthetic experiment which is more realistic than





423 that shown in section 3.1. The 3-D domain has a horizontal extension of 4000 m×4000m  
424 and a vertical extension of 3m. The domain was horizontally discretized into 40×40 grid  
425 cells with a size of 100m×100m and vertically discretized into 30 grid cells with a size  
426 of 0.1m. The domain has a 10% slope in both x and y directions (see Figure 6a). The  
427 parameters of the van Genuchten relationship, porosity and Manning’s coefficient were  
428 set to the same variables for the synthetic experiment in section 3.1.

429

430 The spatially heterogeneous surface saturated hydraulic conductivity was generated  
431 following Kurtz et al. (2016). The field of  $\log_{10}(K_{s,surface})$  was generated by two-  
432 dimensional unconditioned sequential Gaussian simulation. A Gaussian variogram with  
433 nugget, sill, and range values of  $0.0 \log_{10}(\text{m/h})$ ,  $0.1 \log_{10}(\text{m}^2\text{h}^2)$ , and 12 model  
434 grids (1200m), respectively was used to simulate the spatial distribution of  
435  $\log_{10}(K_{s,surface})$ . A constant value of  $-2.30 \log_{10}(\text{m/h})$  (i.e. 0.005 (m/h)) was added  
436 to the generated field. Subsurface saturated hydraulic conductivity was calculated by  
437 equation (3). An ensemble of 51 realizations of  $\log_{10}(K_{s,surface})$  was generated and one  
438 of them was chosen as a synthetic reference (Figure 6a). The remaining 50 members were  
439 used for data assimilation experiments.

440



441 A rainfall rate  $R(x, y)$  (mm/h) was modelled by a logistic function:

$$442 \quad R(x, y) = \frac{R_{max}}{1 + 100 \exp(-0.2 \times \frac{x+y}{2})} \quad (16)$$

443 where  $x$  and  $y$  are horizontal grid numbers ( $1 \leq x \leq 40, 1 \leq y \leq 40$ ). In the synthetic  
444 reference, the maximum rainfall rate in the domain,  $R_{max}$ , was set to 50 (mm/h) (Figure  
445 6b). This rainfall rate was applied for 3 hours and then the period with no rainfall and  
446 evaporation of 0.075mm/h lasted for 117 hours. For data assimilation experiment, an  
447 ensemble of 50 realization of  $R(x, y)$  was generated by adding a lognormal  
448 multiplicative noise to  $R_{max}$  of the synthetic reference. The two parameters of the  
449 lognormal distribution, commonly called  $\mu$  and  $\sigma$ , were set to 0 and 0.15, respectively.

450

451 Figure 6c shows the distribution of surface soil moisture in the synthetic reference run.  
452 Strong rainfall rate applied in the upper part of the slope generates the topography-driven  
453 surface lateral flows. The virtual hourly observations were generated by adding the  
454 Gaussian white noise, whose mean is zero and standard deviation is  $0.05 \text{ m}^3/\text{m}^3$ , to the  
455 volumetric surface soil moisture simulated by the synthetic reference run. Unlike the  
456 experiment in section 3.1, only surface soil moisture can be observed in this synthetic  
457 experiment, which makes this experiment more realistic since satellite sensors can  
458 observe only surface soil moisture. Three different observing networks with different



459 observation densities were used (Figure 7). The observing networks shown in Figure 7a,  
460 7b, and 7c have totally 1, 9, and 361 observations and are called obs1, obs9, and obs361,  
461 respectively.

462

463 In the DA experiments, those virtual observations of surface soil moisture were  
464 assimilated every hour to adjust pressure head and saturated hydraulic conductivity. As I  
465 did in the section 3.1, the NoDA experiments were also implemented. The two different  
466 configurations of ParFlow were used for both DA and NoDA experiments. In the first  
467 configuration, called OF, Parflow explicitly solves overland flows. In the second  
468 configuration, called noOF, Parflow assumes the flat terrain for surface flows so that no  
469 overland flows are generated. Since the synthetic reference run explicitly considers the  
470 topography-driven surface flow, the configuration of noOF assumes that the model  
471 physics is imperfect. I implemented 8 numerical experiments which are summarized in  
472 Table 2. For example, the OF\_DA\_obs9 experiment is the data assimilation experiment  
473 with the observing network shown in Figure 7b, in which Parflow explicitly solves the  
474 topography-driven surface flow. The noOF\_NoDA is the model run without assimilating  
475 observations, in which Parflow does not consider the topography-driven surface flow.

476



477

478 **3.2.2. Results**

479 Figure 8a shows the RMSE of soil moisture simulation of a second soil layer (i.e. 10-  
480 20cm soil depth) in all 8 experiments (the same conclusion described below can be  
481 obtained by analyzing all of shallow soil layers). When Parflow explicitly solves the  
482 topography-driven surface flow, data assimilation substantially reduces RMSE of the soil  
483 moisture simulation (green bars in Figure 8a). The OF\_DA\_obs361 experiment has the  
484 smallest RMSE so that a denser observing network is beneficial to estimate soil moisture.  
485 Figure 8b shows the RMSE of the estimation of saturated surface hydraulic conductivity  
486 in all 8 experiments. Data assimilation also reduces the uncertainty in model's parameters  
487 (green bars in Figure 8b). However, the OF\_DA\_obs361 experiment has larger RMSE  
488 than the other DA experiments. This is because the adjustment of hydraulic conductivity  
489 in the OF\_DA\_obs361 experiment is overfitting to observations. In the OF configuration,  
490 there are two sources of errors, rainfall rate and hydraulic conductivity. However, data  
491 assimilation can adjust only hydraulic conductivity so that the assimilation of a large  
492 number of observations causes overfitting to mitigate the impact of errors in rainfall rate.  
493



494 The noOF\_NoDA experiment has larger RMSE than the OF\_NoDA experiment due to  
495 the negligence of the topography-driven surface flow. In the noOF configuration, data  
496 assimilation also improves the soil moisture simulation (red bars in Figure 8a). The  
497 noOF\_DA\_obs361 experiment outperforms the OF\_NoDA experiment so that data  
498 assimilation with a dense observing network can compensate the negative impact of  
499 neglecting the topography-driven surface flow. Although data assimilation positively  
500 impacts the parameter estimation, the denser observing network cannot reduce RMSE of  
501 hydraulic conductivity estimation (red bars in Figure 8b). The negative impact of the  
502 dense observations in the noOF\_DA\_obs361 experiment on the parameter estimation is  
503 larger than in the OF\_DA\_obs361 experiment. In addition to rainfall rate and hydraulic  
504 conductivity, the imperfect model physics (i.e., no topography-driven surface flow) is the  
505 source of error in the noOF configuration. The assimilation of a large number of  
506 observations causes overfitting because it mitigates the impact of all systematic errors  
507 which comes from three different sources only by adjusting hydraulic conductivity.

508

509 Figure 9 shows the difference of RMSE of the soil moisture simulation between the DA  
510 experiments and the OF\_NoDA experiment. In the DA configuration, the improvement  
511 of the soil moisture estimation can be found in a large area even if there is a single



512 observation in the center of the domain (Figure 9a). Figure 9b shows that the increase of  
513 the number of observations substantially improves the soil moisture simulation in the  
514 region which is affected by topography-driven surface flow (see also Figure 6c). However,  
515 the skill to simulate soil moisture is severely degraded in the lower-left corner of the  
516 domain, which causes the stalled improvement from the OF\_DA\_obs1 experiment to the  
517 OF\_DA\_obs9 experiment shown in Figure 8a. Figure 9c shows that although the far  
518 denser observing network can slightly mitigate this degradation, increasing the number  
519 of observations cannot efficiently solve this issue. This degradation is caused by the  
520 bifurcation of ensemble members at the edge of the area where topography-driven surface  
521 flow reaches (Figure S7). Figure 10 shows KLD in the OF\_NoDA and noOF\_NoDA  
522 experiments. Figure 10a clearly shows that the ensemble simulation generates the strong  
523 non-Gaussianity at the edge of the area where topography-driven surface flow reaches,  
524 which harms the efficiency of the ETKF. This finding is consistent to what I found in the  
525 previous experiment in section 3.1.

526

527 In the noOF configuration, there are large errors in the area around  $500 \leq x, y \leq 1500$   
528 since the increase of soil moisture in this area is caused by the topography-driven surface  
529 flow which is neglected in the noOF configuration. Figures 9d and 9e show that the sparse



530 observations cannot completely remove this degradation caused by imperfect model  
531 physics. Figure 9f shows that the noOF\_DA\_obs361 can outperform the OF\_NoDA  
532 experiment in exchange for the degradation of the parameter estimation as I found in  
533 Figure 8. The unstable behavior of the ETKF found in the OF configuration does not  
534 occur when the topography-driven surface flow is neglected since the ensemble  
535 simulation does not generate the non-Gaussian background distribution (Figure 10b).

536

537

538

#### 539 **4. Discussion**

540 In this study, I revealed that the hyperresolution integrated surface-subsurface  
541 hydrological model gives the unique opportunity to effectively use soil moisture  
542 observations to improve the soil moisture simulation in terms of a horizontal propagation  
543 of observation's information in a model space. I found that the explicit calculation of the  
544 topography-driven surface flow has an important role in propagating the information of  
545 soil moisture observation horizontally by data assimilation even if there is considerable  
546 heterogeneity of meteorological forcing. It is possible that the soil moisture observations



547 in the area where it does not heavily rain can improve the soil moisture simulation in the  
548 severe rainfall area.

549

550 This potential cannot be brought out in the conventional 1-D LSM where sub-grid scale  
551 surface runoff is parameterized and the surface flows in one grid do not move to the  
552 adjacent grids. Neglecting the topography-driven surface flow causes significant bias in  
553 the soil moisture simulation and this bias cannot be completely mitigated by data  
554 assimilation especially in the case of a sparse observing network. However, I found that  
555 even if the model uses imperfect physics which neglects the interaction between  
556 topography-driven surface lateral flows and subsurface soil moisture, assimilating soil  
557 moisture observations into the model's three-dimensional state and parameter space can  
558 improve the skill to estimate soil moisture and hydraulic conductivity. This finding  
559 implies that the conventional 1-D LSM with full 3-D data assimilation may be a  
560 computationally cheap and reasonable choice in some cases although many land data  
561 assimilation systems with the conventional 1-D LSM currently update state variables only  
562 in a single model's horizontal grid which is identical to the location of the observation.

563





564 The conventional ensemble data assimilation (i.e. ETKF) severely suffers from the non-  
565 Gaussian background error PDFs caused by the strongly nonlinear dynamics of the  
566 topography-driven surface flow. The efficiency of ETKF to propagate the information of  
567 observations horizontally in the model space is limited in the edge of the area where the  
568 topography-driven surface flow reaches. Please note that the low representativeness of  
569 the soil moisture observations in the case of the HIGH\_K reference shown in section 3.1  
570 is due to the core assumption of the Kalman filter that the error PDFs follow the Gaussian  
571 distribution so that the increase of the ensemble size cannot solve this issue. I  
572 implemented the data assimilation experiment in the case of the HIGH\_K reference with  
573 an ensemble size of 500, which is 10 times larger than the original experiments shown in  
574 section 3.1, and found no significant improvement of the soil moisture simulation (not  
575 shown). Some studies revealed that volumetric soil moisture distributions follow the  
576 Gaussian distribution better than pressure head so that they recommend to update soil  
577 moisture as a state variable (e.g., Zhang et al. (2018)). However, in this study, I found that  
578 volumetric soil moisture distributions have bimodal structure and do not follow the  
579 Gaussian distribution. The limitation of ensemble Kalman filters found in this study does  
580 not depend on the updated state variables.

581



582 The spatially dense soil moisture observations are needed to efficiently constrain state  
583 variables at the edge of surface flows. High resolution soil moisture remote sensing based  
584 on satellite active and passive combined microwave observations at the 1 km spatial  
585 resolution (e.g., He et al. 2018) and the assimilation of those data (Lievens et al. 2017)  
586 may be important in the era of the hyperresolution land modeling. High resolution  
587 observations of surface inundated water from satellite imagery with a spatial resolution  
588 finer than 100 m (e.g., Sakamoto et al. 2007; Arnesen et al. 2013) may also be useful.  
589 However, the numerical experiment in section 3.2 implies that the dense observing  
590 network of surface soil moisture cannot completely remove the negative impact of the  
591 non-Gaussian background PDF.

592

593 Since there is a nonlinear relationship between observed and unobserved variables  
594 sampled by an ensemble, a localization method, which spatially restricts the impact of  
595 assimilating observations, is crucially needed for real-world applications. The results of  
596 this study imply that the optimal localization radius strongly depends on the model  
597 parameter (i.e. saturated hydraulic conductivity). Rasmussen et al. (2015) successfully  
598 applied the adaptive localization method (Anderson 2007; Bishop and Hodyss 2009) to  
599 the data assimilation of groundwater observations into a hydrological model. It is



600 appropriate to adaptively determine the localization radius considering the lack of prior  
601 knowledge of how soil moisture simulated by an ensemble is horizontally correlated.  
602  
603 Reducing the uncertainty in rainfall positively impacts the efficiency of data assimilation  
604 since the bifurcation of simulated soil moisture found in Figure 5c is originally induced  
605 by the uncertainty in rainfall. Although assimilating land hydrological observations to  
606 improve the rainfall input has been intensively investigated (e.g., Sawada et al. 2018;  
607 Herrnegger et al. 2015; Crow et al. 2011; Vrugt et al. 2008), it has yet to be applied to  
608 hyperresolution land models. Please note that the parameters of the lognormal distribution  
609 to model the uncertainty in rainfall were specified to make the rainfall PDF similar to the  
610 Gaussian distribution. I chose the lognormal distribution in order not to generate negative  
611 rainfall values and I intended not to introduce non-Gaussianity into the external forcing.  
612 The rainfall input which follows the Gaussian PDF was transformed into the non-  
613 Gaussian PDF of the background error by the strongly nonlinear dynamics of the  
614 topography-driven surface flow.  
615  
616 To explicitly consider non-Gaussianity and non-linear relationship between observed and  
617 unobserved variables induced by the topography-driven surface flow, the particle filters



618 may be useful. The particle filter can represent a probability distribution (including non-  
619 Gaussian distributions) directly by an ensemble. Particle filters have been intensively  
620 applied to conventional 1-D LSMs (e.g., Sawada et al. 2015; Qin et al. 2009) and lumped  
621 hydrological models (e.g., Yan and Moradkhani 2016; Vrugt et al. 2013). Although  
622 particle filtering in a high dimensional system suffers from the “curse of dimensionality”  
623 (e.g., Snyder et al. 2008), the applicability of particle filtering to 3-D hyperresolution land  
624 models should be assessed in the future.

625

626 Since the synthetic numerical experiments in this paper adopted the simple and  
627 minimalistic setting, the findings of this paper may be exaggerated. There are no river  
628 channels in the synthetic experiment so that the skill to simulate river water level and  
629 discharge cannot be discussed, which is the major limitation of this study. The simple  
630 representation of soil properties is also a limitation of this study. In future work, the  
631 contributions of the topography-driven surface runoff process to the data assimilation of  
632 hydrological observations should be quantified in real-world applications. In addition, in  
633 the virtual experiment of this paper, I neglected some of the important land processes such  
634 as transpiration, canopy interception, snow, and frozen soil. Although they are generally  
635 not primary factors in the propagation of overland flows generated by extreme rainfall,



636 which has a shorter timescale than the neglected processes, those processes should be  
637 considered in the future.

638

639

## 640 **5. Conclusions**

641 The simplified synthetic experiments of this study indicate that topography-driven lateral  
642 surface flows induced by heavy rainfalls do matter for data assimilation of hydrological  
643 observations into hyperresolution land models. Even if there is extreme heterogeneity of  
644 rainfall, the information of soil moisture observations can be propagated horizontally in  
645 the model space and the soil moisture simulation can be improved by the ensemble  
646 Kalman filter. However, the nonlinear dynamics of the topography-driven surface flow  
647 induces the non-Gaussianity of the model error, which harms the efficiency of data  
648 assimilation of soil moisture observations. It is difficult to efficiently constrain model  
649 states at the edge of the area where the topography-driven surface flow reaches by linear-  
650 Gaussian filters, which brings the new challenge in land data assimilation for  
651 hyperresolution land models.

652

## 653 **Acknowledgement**



654 This study was supported by the JSPS KAKENHI grant JP17K18352 and 18H03800.

655

#### 656 **Code/Data Availability**

657 All data used in this paper are stored in the repository of the University of Tokyo for 5  
658 years and available upon request to the author. The ETKF code used in this study can be  
659 found at <https://github.com/takemasa-miyoshi/letkf>.

660

#### 661 **Author Contribution**

662 YS designed the study, executed numerical experiments, analyzed the results, and wrote  
663 the paper.

664

#### 665 **Competing interests**

666 The author declares no competing interests.

667

#### 668 **References**

669

670 Ait-El-Fquih, B., El Gharamti, M., and Hoteit, I.: A Bayesian consistent dual ensemble  
671 Kalman filter for state-parameter estimation in subsurface hydrology. *Hydrology and*



672 *Earth System Sciences*, 20(8), 3289–3307. <https://doi.org/10.5194/hess-20-3289-2016>,

673 2016

674

675 Amesen et al.: Monitoring flood extent in the lower Amazon River floodplain using

676 ALOS/PALSAR ScanSAR images. *Remote Sensing of Environment*, 130, 51–61.

677 <https://doi.org/10.1016/j.rse.2012.10.035>, 2013

678

679 Anderson, J. L.: Exploring the need for localization in ensemble data assimilation using

680 a hierarchical ensemble filter. *Physica D: Nonlinear Phenomena*, 230(1–2), 99–111.

681 <https://doi.org/10.1016/j.physd.2006.02.011>, 2007

682

683 Bandara, R., Walker, J. P., and Rüdiger, C.: Towards soil property retrieval from space:

684 Proof of concept using in situ observations. *Journal of Hydrology*, 512, 27–38.

685 <https://doi.org/10.1016/j.jhydrol.2014.02.031>, 2014

686

687 Bandara, R., Walker, J. P., Rüdiger, C., and Merlin, O.: Towards soil property retrieval

688 from space: An application with disaggregated satellite observations. *Journal of*

689 *Hydrology*, 522, 582–593, <https://doi.org/10.1016/j.jhydrol.2015.01.018>, 2015



690

691 Beven, K.: On subsurface stormflow: an analysis of response times, *Hydrological Science*  
692 *Journal*, 27, 505-521, doi:10.1080/02626668209491129, 1982

693

694 Bishop, C.H., Etherton, B., J., and Majumdar, S., J.: Adaptive Sampling with the  
695 Ensemble Transform Kalman Filter. Part I: Theoretical Aspects. *Monthly. Weather.*  
696 *Review.*, **129**, 420–436, [https://doi.org/10.1175/1520-](https://doi.org/10.1175/1520-0493(2001)129<0420:ASWTET>2.0.CO;2)  
697 [0493\(2001\)129<0420:ASWTET>2.0.CO;2](https://doi.org/10.1175/1520-0493(2001)129<0420:ASWTET>2.0.CO;2), 2001.

698

699 Bishop, C. H., and Hodyss, D.: Ensemble covariances adaptively localized with ECO-  
700 RAP. Part 1: Tests on simple error models. *Tellus*, 61A, 84–96,  
701 <https://doi.org/10.1111/j.1600-0870.2008.00371.x>, 2009.

702

703 Camporese, M., Paniconi, C., Putti, M., and Salandin, P.: Ensemble Kalman filter data  
704 assimilation for a process-based catchment scale model of surface and subsurface flow.  
705 *Water Resources Research*, 45(10), 1–14. <https://doi.org/10.1029/2008WR007031>, 2009.

706





707 Camporese, M., Paniconi, C., Putti, M., and Orlandini, S.: Surface-subsurface flow  
708 modeling with path-based runoff routing, boundary condition-based coupling, and  
709 assimilation of multisource observation data. *Water Resources Research*, 46(2).  
710 <https://doi.org/10.1029/2008WR007536>, 2010.

711

712 Crow, W. T., Van Den Berg, M. J., Huffman, G. J., and Pellarin, T.: Correcting rainfall  
713 using satellite-based surface soil moisture retrievals: The Soil Moisture Analysis Rainfall  
714 Tool (SMART). *Water Resources Research*, 47(8), 1–15.  
715 <https://doi.org/10.1029/2011WR010576>, 2011.

716

717 Fang, Y., L. R. Leung, Z. Duan, M. S. Wigmosta, R. M. Maxwell, J. Q. Chambers, and J.  
718 Tomasella: Influence of landscape heterogeneity on water available to tropical forests in  
719 an Amazonian catchment and implications for modeling drought response, *J. Geophys.*  
720 *Res. Atmos.*, 122, <https://doi.org/10.1002/2017JD027066>, 2017.

721

722 Han, X., Franssen, H.-J. H., Montzka, C. and Vereecken, H.: Soil moisture and soil  
723 properties estimation in the Community Land Model with synthetic brightness



724 temperature observations, *Water Resources Research*, 50, 6081 - 6105,

725 <https://doi.org/10.1002/2013WR014586>, 2014

726

727 Hernegger, M., Nachtnebel, H. P., and Schulz, K.: From runoff to rainfall : inverse

728 rainfall – runoff modelling in a high temporal resolution, 4619–4639.

729 <https://doi.org/10.5194/hess-19-4619-2015>, 2015

730

731 He, L., Hong, Y., Wu, X., Ye, N., Walker, J. P. and Chen, X.: Investigation of SMAP

732 Active–Passive Downscaling Algorithms Using Combined Sentinel-1 SAR and SMAP

733 Radiometer Data. *IEEE Transactions on Geosciences and Remote Sensing*, 56, 4906-

734 4918, <https://doi.org/10.1109/TGRS.2018.2842153>, 2018

735

736 Hendricks Franssen, H. J., and Kinzelbach, W.: Real-time groundwater flow modeling

737 with the Ensemble Kalman Filter: Joint estimation of states and parameters and the filter

738 inbreeding problem. *Water Resources Research*, 44(9), 1–21.

739 <https://doi.org/10.1029/2007WR006505>, 2008

740



- 741 Houborg, R., Rodell, M., Li, B., Reichle, R., and Zaitchik, B. F.: Drought indicators based  
742 on model-assimilated Gravity Recovery and Climate Experiment (GRACE) terrestrial  
743 water storage observations. *Water Resources Research*, 48(7).  
744 <https://doi.org/10.1029/2011WR011291>, 2012  
745
- 746 Houtekamer, P. L., and Zhang, F.: Review of the Ensemble Kalman Filter for Atmospheric  
747 Data Assimilation. *Monthly Weather Review*, MWR-D-15-0440.1.  
748 <https://doi.org/10.1175/MWR-D-15-0440.1>, 2016  
749
- 750 Hunt, B. R., Kostelich, E. J., and Szunyogh, I.: Efficient data assimilation for  
751 spatiotemporal chaos: A local ensemble transform Kalman filter. *Physica D: Nonlinear*  
752 *Phenomena*, 230(1–2), 112–126. <https://doi.org/10.1016/j.physd.2006.11.008>, 2007  
753
- 754 Ji, P., Yuan, X., and Liang, X. Z.: Do Lateral Flows Matter for the Hyperresolution Land  
755 Surface Modeling? *Journal of Geophysical Research: Atmospheres*, 1–16.  
756 <https://doi.org/10.1002/2017JD027366>, 2017  
757



758 Keune, J., F. Gasper, K. Goergen, A. Hense, P. Shrestha, M. Sulis, and S. Kollet: Studying  
759 the influence of groundwater representations on land surface-atmosphere feedbacks  
760 during the European heat wave in 2003, *Journal of Geophysical Research. Atmospheres*,  
761 121, 13,301–13,325, <https://doi.org/10.1002/2016JD025426>, 2016.

762

763 Kollet, S. J., and Maxwell, R. M.: Integrated surface–groundwater flow modeling: A free-  
764 surface overland flow boundary condition in a parallel groundwater flow model.  
765 *Advances in Water Resources*, 29(7), 945–958.  
766 <https://doi.org/10.1016/j.advwatres.2005.08.006>, 2006.

767

768 Kumar, S. V., Reichle, R. H., Koster, R. D., Crow, W. T., and Peters-Lidard, C. D.: Role  
769 of Subsurface Physics in the Assimilation of Surface Soil Moisture Observations. *Journal*  
770 *of Hydrometeorology*, 10(6), 1534–1547. <https://doi.org/10.1175/2009JHM1134.1>, 2009

771

772 Kurtz, W., He, G., Kollet, S. J., Maxwell, R. M., Vereecken, H., and Franssen, H. J. H.:  
773 TerrSysMP-PDAF (version 1.0): A modular high-performance data assimilation  
774 framework for an integrated land surface-subsurface model. *Geoscientific Model*  
775 *Development*, 9(4), 1341–1360. <https://doi.org/10.5194/gmd-9-1341-2016>, 2016.



776

777 Kullback, S., and Leibler, R. A.: On information and sufficiency, *The Annals of*  
778 *Mathematical Statistics*, 22, 79-86, 1951.

779

780 Lawrence, D. M., et al.: Parameterization improvements and functional and structural  
781 advances in Version 4 of the Community Land Model. *Journal of Advances in Modeling*  
782 *Earth Systems*, 3(3), 1–27. <https://doi.org/10.1029/2011MS000045>, 2011

783

784 Li, B., Rodell, M., Zaitchik, B. F., Reichle, R. H., Koster, R. D., and van Dam, T. M.:  
785 Assimilation of GRACE terrestrial water storage into a land surface model: Evaluation  
786 and potential value for drought monitoring in western and central Europe. *Journal of*  
787 *Hydrology*, 446–447, 103–115. <https://doi.org/10.1016/j.jhydrol.2012.04.035>, 2012

788

789 Lievens, et al.: Joint Sentinel-1 and SMAP data assimilation to improve soil moisture  
790 estimates. *Geophysical Research Letters*, 44(12), 6145–6153.  
791 <https://doi.org/10.1002/2017GL073904>, 2017.

792



793 Martens, B., Miralles, D. G., Lievens, H., Schalie, R. Van Der, and Jeu, R. A. M. De.:

794 GLEAM v3 : satellite-based land evaporation and root-zone soil moisture, *Geoscientific*

795 *Model Development*, 10, 1903–1925. <https://doi.org/10.5194/gmd-10-1903-2017>, 2017

796

797 Maxwell, R. M., and N. L. Miller: Development of a Coupled Land Surface and

798 Groundwater Model. *Journal of Hydrometeorology*, 6, 233-247.

799 <https://doi.org/10.1175/JHM422.1>, 2005

800

801 Maxwell, R. M., and Condon, L. E.: Connections between groundwater flow and

802 transpiration partitioning. *Science*, 353, 377-380, <https://doi.org/10.1126/science.aaf7891>,

803 2016

804

805 Maxwell, R. M., Condon, L. E., and Kollet, S. J.: A high-resolution simulation of

806 groundwater and surface water over most of the continental US with the integrated

807 hydrologic model ParFlow v3, 923–937. <https://doi.org/10.5194/gmd-8-923-2015>, 2015.

808



809 Maxwell, R. M., and Kollet, S. J.: Interdependence of groundwater dynamics and land-  
810 energy feedbacks under climate change, *Nature Geoscience*, *1*, 665–669.  
811 <https://doi.org/10.1038/ngeo315>, 2008.

812

813 Maxwell, R. M., Lundquist, J. K., Mirocha, J. D., Smith, S. G., Woodward, C. S., and  
814 Tompson, A. F. B.: Development of a Coupled Groundwater–Atmosphere Model.  
815 *Monthly Weather Review*, *139*(1), 96–116. <https://doi.org/10.1175/2010MWR3392.1>,  
816 2011

817

818 Nerger, L., and Hiller, W.,: Software for ensemble-based data assimilation systems –  
819 implementation strategies and scalability. *Computers and Geosciences*. *55*, 110–118.  
820 <https://doi.org/10.1016/j.cageo.2012.03.026>, 2013

821

822 Niu, G. Y., Paniconi, C., Troch, P. a., Scott, R. L., Durcik, M., Zeng, X., and Goodrich, D.  
823 C.: An integrated modelling framework of catchment-scale ecohydrological processes: 1.  
824 Model description and tests over an energy-limited watershed. *Ecohydrology*, *7*(2), 427–  
825 439. <https://doi.org/10.1002/eco.1362>, 2014

826



- 827 Paloscia, S, Pettinato, S., Santi, E., Notarnicola, C., Pasolli, L., and Reppucci, A.: Soil  
828 moisture mapping using Sentinel-1 images: Algorithm and preliminary validation.  
829 *Remote Sensing of Environment*, 134, 234-248. <https://doi.org/10.1016/j.rse.2013.02.027>,  
830 2013.
- 831
- 832 Pokhrel, P., and Gupta, H. V.: On the use of spatial regularization strategies to improve  
833 calibration of distributed watershed models. *Water Resources Research*, 46(1), 1–17.  
834 <https://doi.org/10.1029/2009WR008066>, 2010
- 835
- 836 Qin, J., Liang, S., Yang, K., Kaihotsu, I., Liu, R., and Koike, T.: Simultaneous estimation  
837 of both soil moisture and model parameters using particle filtering method through the  
838 assimilation of microwave signal. *Journal of Geophysical Research*, 114(D15), 1–13.  
839 <https://doi.org/10.1029/2008JD011358>, 2009.
- 840
- 841 Rasmussen, J., Madsen, H., Jensen, K. H., and Refsgaard, J. C.: Data assimilation in  
842 integrated hydrological modeling using ensemble Kalman filtering: evaluating the effect  
843 of ensemble size and localization on filter performance. *Hydrology and Earth System*  
844 *Sciences*, 19(7), 2999–3013. <https://doi.org/10.5194/hess-19-2999-2015>, 2015.





845

846 Ridler, M.-E., H. Madsen, S. Stisen,, S. Bircher, and R. Fensholt, Assimilation of SMOS-  
847 derived soil moisture in a fully integrated hydrological and soil-vegetation-atmosphere  
848 transfer model in Western Denmark, *Water Resour. Res.*, *50*, 8962 - 8981,  
849 <https://doi.org/10.1002/2014WR015392>, 2014.

850

851 Sakamoto, T., et al.: Detecting temporal changes in the extent of annual flooding within  
852 the Cambodia and the Vietnamese Mekong Delta from MODIS time-series imagery.  
853 *Remote Sensing of Environment*, *109*, 295-313.  
854 <https://doi.org/10.1016/j.rse.2007.01.011>, 2007.

855

856 Sawada, Y. and Koike, T.: Simultaneous estimation of both hydrological and ecological  
857 parameters in an eco-hydrological model by assimilating microwave signal, *Journal of*  
858 *Geophysical Research – Atmospheres*, *119*, 8839-8857,  
859 <https://doi.org/10.1002/2014JD021536>, 2014.

860



861 Sawada, Y., Koike, T., and Walker, J. P.: A land data assimilation system for simultaneous  
862 simulation of soil moisture and vegetation dynamics, *Journal of Geophysical Research –*  
863 *Atmospheres*, 120, 5910-5930, <https://doi.org/10.1002/2014JD022895>, 2015  
864  
865 Sawada, Y., Nakaegawa, T., and Miyoshi, T.: Hydrometeorology as an inversion problem:  
866 Can river discharge observations improve the atmosphere by ensemble data assimilation?,  
867 *Journal of Geophysical Research - Atmospheres*, 123, 848-860,  
868 <https://doi.org/10.1002/2017JD027531>, 2018  
869  
870 Sellers, P. J., et al.: A revised land surface parameterization (SiB2) for atmospheric GCMs.  
871 Part I: Model formulation. *Journal of Climate*. [https://doi.org/10.1175/1520-](https://doi.org/10.1175/1520-0442(1996)009<0676:ARLSPF>2.0.CO;2)  
872 [0442\(1996\)009<0676:ARLSPF>2.0.CO;2](https://doi.org/10.1175/1520-0442(1996)009<0676:ARLSPF>2.0.CO;2), 1996  
873  
874 Shrestha, P., Sulis, M., Masbou, M., Kollet, S., and Simmer, C.: A Scale-Consistent  
875 Terrestrial Systems Modeling Platform Based on COSMO, CLM, and ParFlow. *Monthly*  
876 *Weather Review*, 142(9), 3466–3483. <https://doi.org/10.1175/MWR-D-14-00029.1>, 2014  
877



- 878 Snyder, C., Bengtsson, T., Bickel, P., and Anderson, J.: Obstacles to High-Dimensional  
879 Particle Filtering. *Monthly Weather Review*, 136(12), 4629–4640.  
880 <https://doi.org/10.1175/2008MWR2529.1>, 2008  
881  
882 Tian, W., Li, X., Cheng, G. D., Wang, X. S., and Hu, B. X.: Coupling a groundwater  
883 model with a land surface model to improve water and energy cycle simulation.  
884 *Hydrology and Earth System Sciences*, 16(12), 4707–4723. [https://doi.org/10.5194/hess-](https://doi.org/10.5194/hess-16-4707-2012)  
885 [16-4707-2012](https://doi.org/10.5194/hess-16-4707-2012), 2012.  
886  
887 Van Genuchten, M. T.: A closed-form equation for predicting the hydraulic conductivity  
888 of unsaturated soils, *Soil Science Society of America Journal*, 44, 892–898, 1980.  
889  
890 Verbeeck, H., Peylin, P., Bacour, C., Bonal, D., Steppe, K., and Ciais, P.: Fluxes in  
891 Amazon forests: Fusion of eddy covariance data and the ORCHIDEE model. *Journal of*  
892 *Geophysical Research*, 116(G2), 1–19. <https://doi.org/10.1029/2010JG001544>, 2011.  
893  
894 Vrugt, J. A., ter Braak, C. J. F., Clark, M. P., Hyman, J. M., and Robinson, B. A.:  
895 Treatment of input uncertainty in hydrologic modeling: Doing hydrology backward with



896 Markov chain Monte Carlo simulation. *Water Resources Research*, 44, 1–15.

897 <https://doi.org/10.1029/2007WR006720>, 2008.

898

899 Vrugt, J. A., ter Braak, C. J. F., Diks, C. G. H., and Schoups, G.: Hydrologic data

900 assimilation using particle Markov chain Monte Carlo simulation: Theory, concepts and

901 applications. *Advances in Water Resources*, 51, 457–478.

902 <https://doi.org/10.1016/j.advwatres.2012.04.002>, 2013.

903

904 Williams, J. L., and Maxwell, R. M.: Propagating Subsurface Uncertainty to the

905 Atmosphere Using Fully Coupled Stochastic Simulations. *Journal of Hydrometeorology*,

906 12(4), 690–701. <https://doi.org/10.1175/2011JHM1363.1>, 2011.

907

908 Wood, E. F., et al.: Hyperresolution global land surface modeling : Meeting a grand

909 challenge for monitoring Earth’s terrestrial water, *Water Resources Research*, 47,

910 <https://doi.org/10.1029/2010WR010090>, 2011.

911



- 912 Yan, H., and Moradkhani, H.: Combined assimilation of streamflow and satellite soil  
913 moisture with the particle filter and geostatistical modeling. *Advances in Water Resources*,  
914 *94*, 364–378. <https://doi.org/10.1016/j.advwatres.2016.06.002>, 2016.
- 915
- 916 Yang, K., Koike, T., Kaihotsu, I., and Qin, J.: Validation of a Dual-Pass Microwave Land  
917 Data Assimilation System for Estimating Surface Soil Moisture in Semiarid Regions.  
918 *Journal of Hydrometeorology*, *10*(3), 780–793. <https://doi.org/10.1175/2008JHM1065.1>,  
919 2009.
- 920
- 921 Yang, K., Watanabe, T., Koike, T., Li, X., Fujii, H., Tamagawa, K., and Ishikawa, H.:  
922 Auto-calibration System Developed to Assimilate AMSR-E Data into a Land Surface  
923 Model for Estimating Soil Moisture and the Surface Energy Budget. *Journal of the*  
924 *Meteorological Society of Japan*, *85A*, 229–242. <https://doi.org/10.2151/jmsj.85A.229>,  
925 2007.
- 926
- 927 Zhang, D., Madsen, H., Ridler, M. E., Refsgaard, J. C., and Jensen, K. H.: Impact of  
928 uncertainty description on assimilating hydraulic head in the MIKE SHE distributed



929 hydrological model, *Advances in Water Resources*, 86, 400–413,

930 <https://doi.org/10.1016/j.advwatres.2015.07.018>, 2015.

931

932 Zhang, F., Snyder, C., and Sun, J.: Impacts of Initial Estimate and Observation

933 Availability on Convective-Scale Data Assimilation with an Ensemble Kalman Filter.

934 *Monthly. Weather. Review.*, **132**, 1238–1253, <https://doi.org/10.1175/1520->

935 [0493\(2004\)132<1238:IOIEAO>2.0.CO;2](https://doi.org/10.1175/1520-0493(2004)132<1238:IOIEAO>2.0.CO;2), 2004

936

937 Zhang, H., Kurtz, W., Kollet, S., Vereecken, H., and Franssen, H. J. H.: Comparison of

938 different assimilation methodologies of groundwater levels to improve predictions of root

939 zone soil moisture with an integrated terrestrial system model. *Advances in Water*

940 *Resources*, *111*, 224–238. <https://doi.org/10.1016/j.advwatres.2017.11.003>, 2018.

941

942



943

944

945

946 **Table 1.** Configuration of the data assimilation experiments in section 3.1.

	hydraulic conductivity [m/h]	observation's location [m]
LOW_K-UP_O	0.005	2500
LOW_K-DOWN_O	0.005	1500
HIGH_K-UP_O	0.02	2500
HIGH_K-DOWN_O	0.02	1500

947

948 **Table 2.** Configuration of the data assimilation experiments in section 3.2

	overland flows	observing network
noOF_NoDA	none	no data assimilation
noOF_DA_obs1	none	Figure 7a
noOF_DA_obs9	none	Figure 7b
noOF_DA_obs361	none	Figure 7c
OF_NoDA	simulated	no data assimilation
OF_DA_obs1	simulated	Figure 7a
OF_DA_obs9	simulated	Figure 7b
OF_DA_obs361	simulated	Figure 7c

949

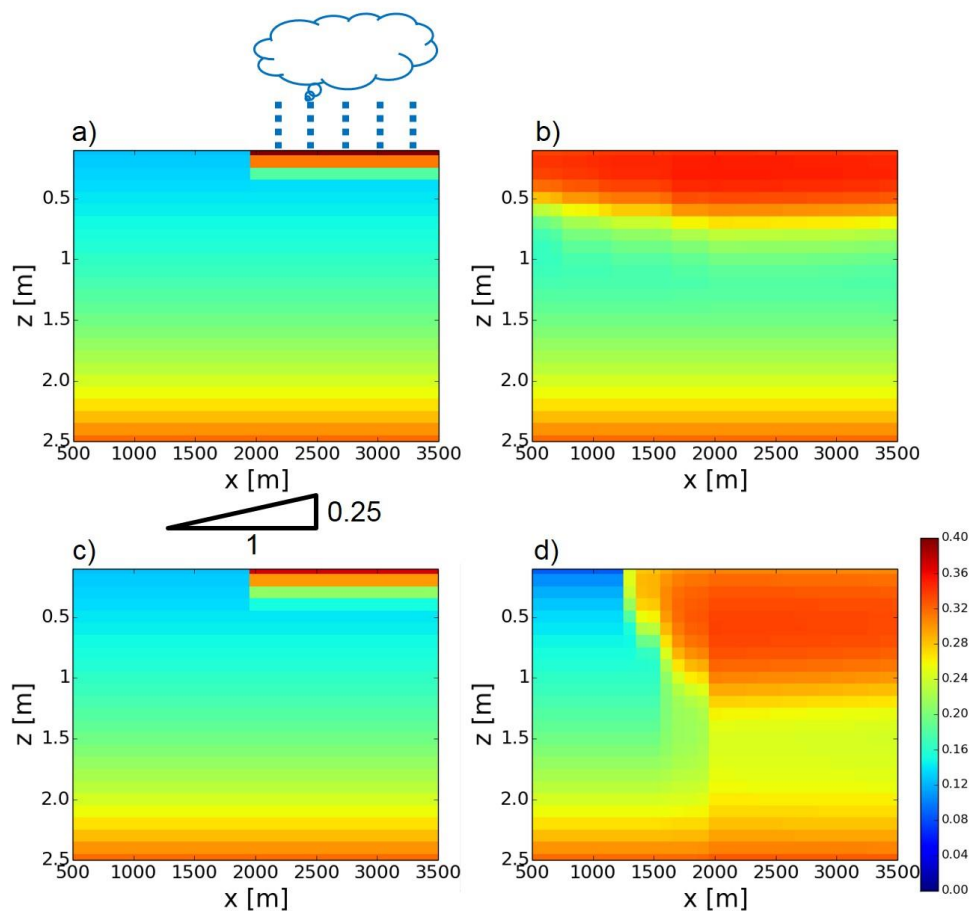
950

951

952



953

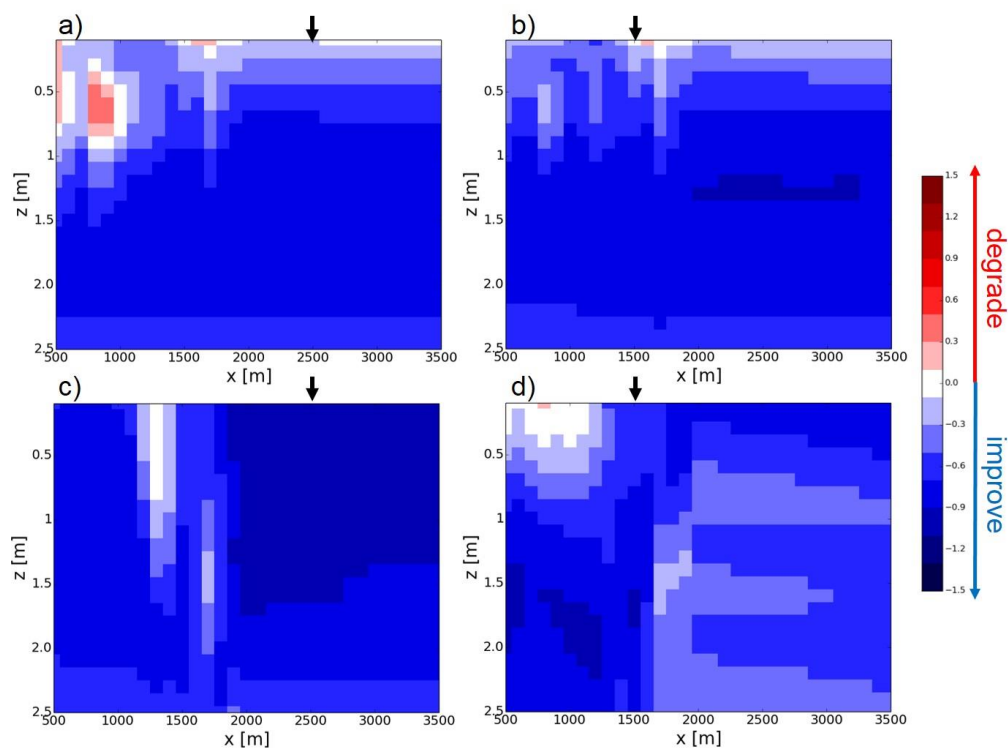


954

955 **Figure 1.** Distributions of volumetric soil moisture simulated by the synthetic reference runs. (a) The  
956 distribution of volumetric soil moisture [ $\text{m}^3/\text{m}^3$ ] simulated by the LOW\_K synthetic reference run at  $t = 0\text{h}$ .  
957 The schematic of the configuration of the synthetic reference runs is also shown (see also section 3). (b) same  
958 as (a) but at  $t = 130\text{h}$ . (c,d) same as (a,b) but for the HIGH\_K synthetic reference run.

959





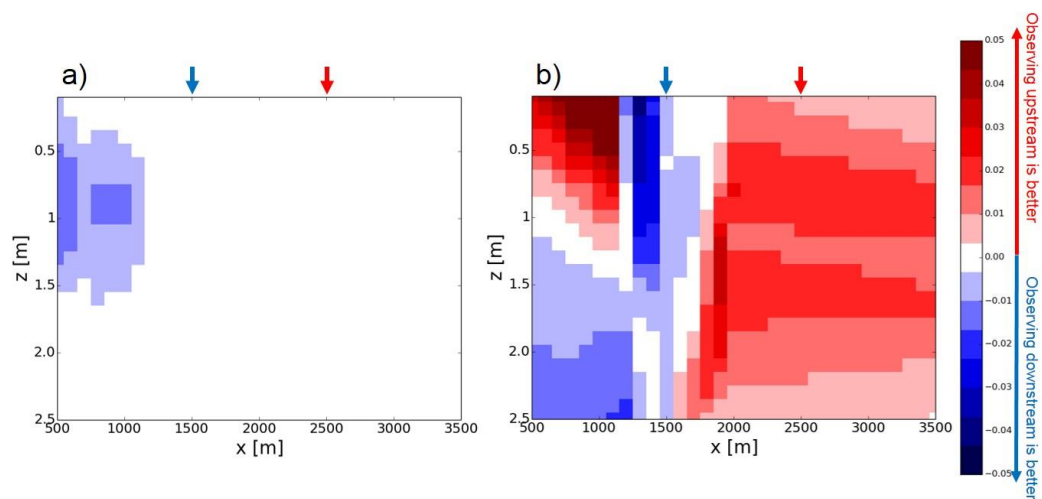
960

961 **Figure 2.** The improvement rates of the (a) LOW\_K-UP\_O, (b) LOW\_K-DOWN\_O, (c) HIGH\_K\_UP\_O,

962 (d) HIGH\_K-DOWN\_O experiments (see Table 1 and section 3). Black arrows show the locations of the soil

963 moisture observations in each experiment.

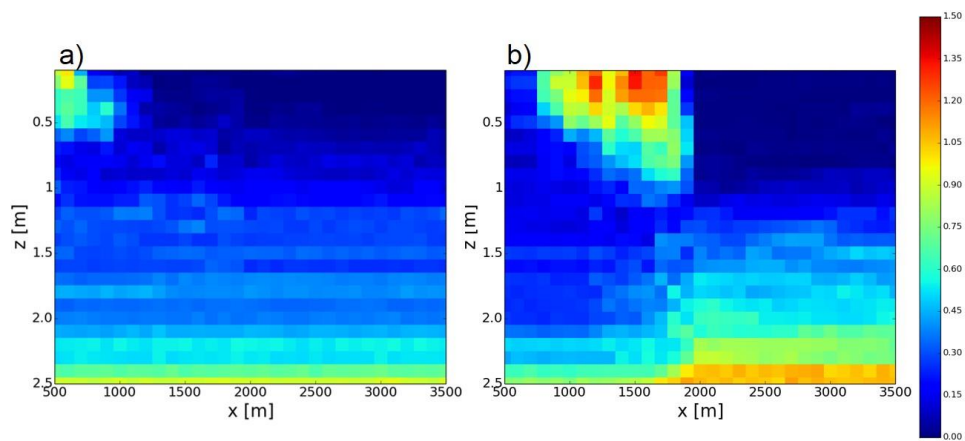
964



965

966 **Figure 3.** (a) The difference of time-mean RMSEs between the LOW\_K-UP\_O and LOW\_K-DOWN\_O  
967 experiments (see Table 1 and section 3). Red (blue) color indicates that the observations in the upper (lower)  
968 part of the slope reduce time-mean RMSE by data assimilation better than those in the lower (upper) part of  
969 the slope (see also arrows which are the locations of the observations). (b) same as (a) but for the difference  
970 between the HIGH\_K-UP\_O and HIGH\_K-DOWN\_O experiments.

971

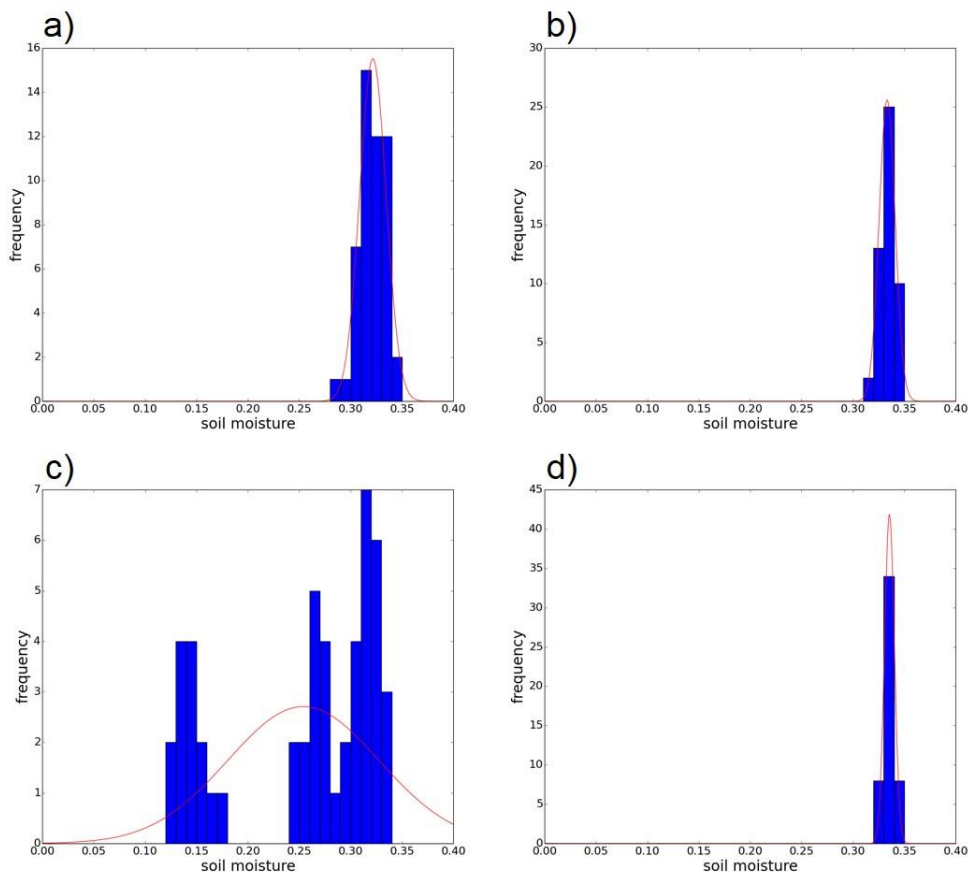


972

973 **Figure 4.** The Kullback-Leibler divergence of the NoDA experiment generated by (a) the LOW\_K reference

974 and (b) the HIGH\_K reference at  $t = 130\text{h}$  (see also Figure 1b and 1d).

975



976

977 **Figure 5.** (a) The histogram (blue bars) of the volumetric soil moisture simulated by the NoDA experiment

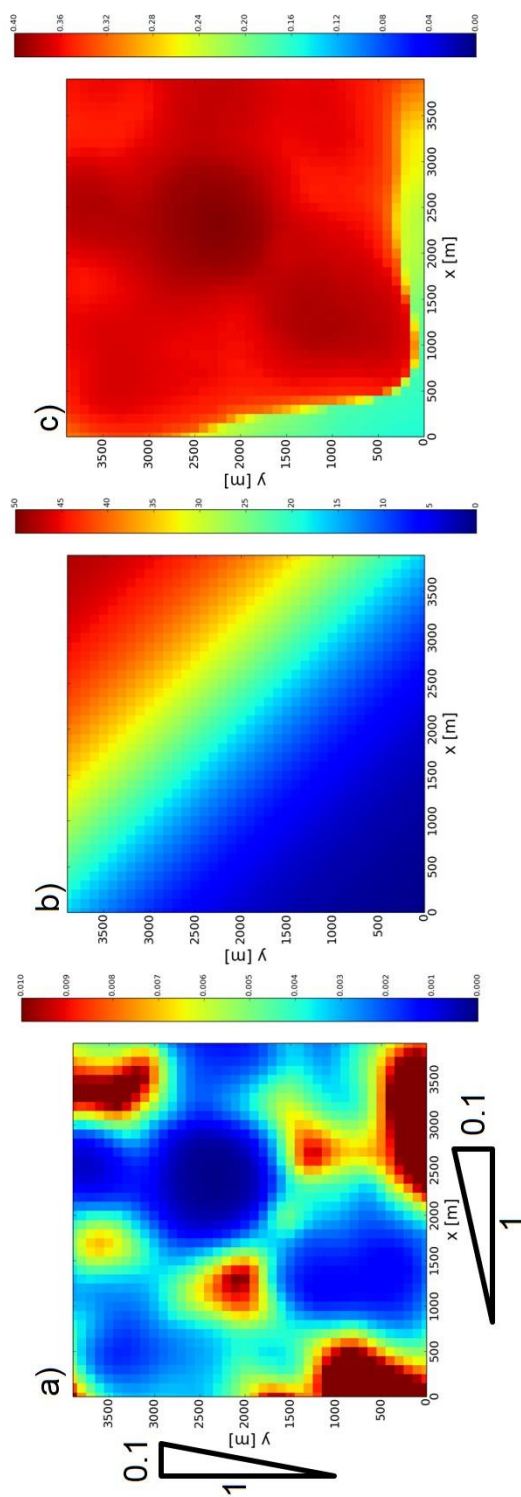
978 (see section 3) with the LOW\_K reference at  $x=1500\text{m}$ ,  $z=0.5\text{m}$ , and  $t=130\text{h}$  (see also Figure 4). Red line

979 shows the Gaussian distribution with the mean and variance sampled by the ensemble. (b) same as (a) but at

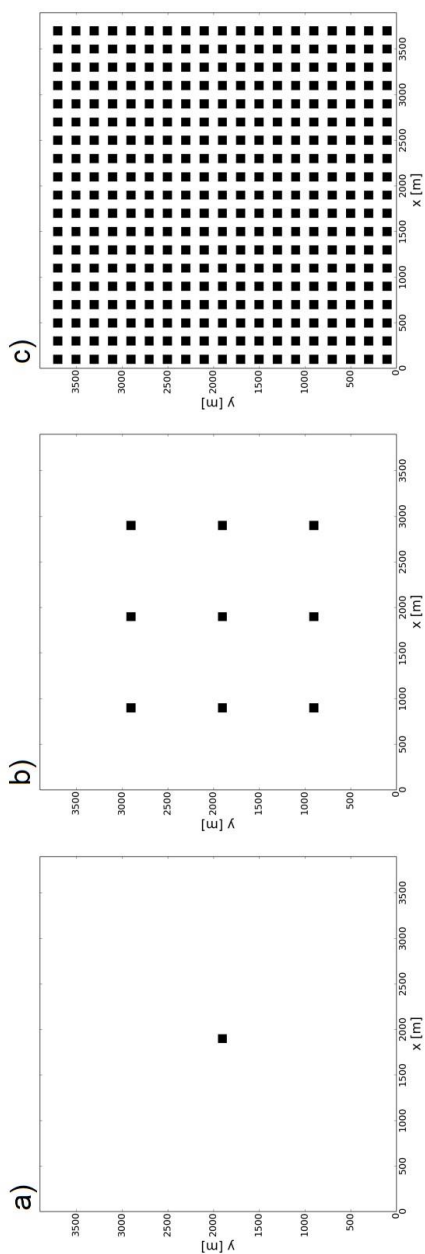
980  $x=2500\text{m}$ ,  $z=0.5\text{m}$ , and  $t=130\text{h}$ . (c) same as (a) but for the HIGH\_K reference. (d) same as (c) but at  $x=2500\text{m}$ ,

981  $z=0.5\text{m}$ , and  $t=130\text{h}$ .

982



984 **Figure 6.** (a) Distribution of surface saturated hydraulic conductivity [m/h] in the synthetic reference. (b) Distribution of rainfall rate [mm/h] in the synthetic  
985 reference. (c) Surface volumetric soil moisture [m<sup>3</sup>/m<sup>3</sup>] at t = 5 [h] in the synthetic reference.



988 **Figure 7.** Observing networks. Black boxes are observed grids. (a) obs1, (b) obs9, (c) obs361 See also section 3.2.1.

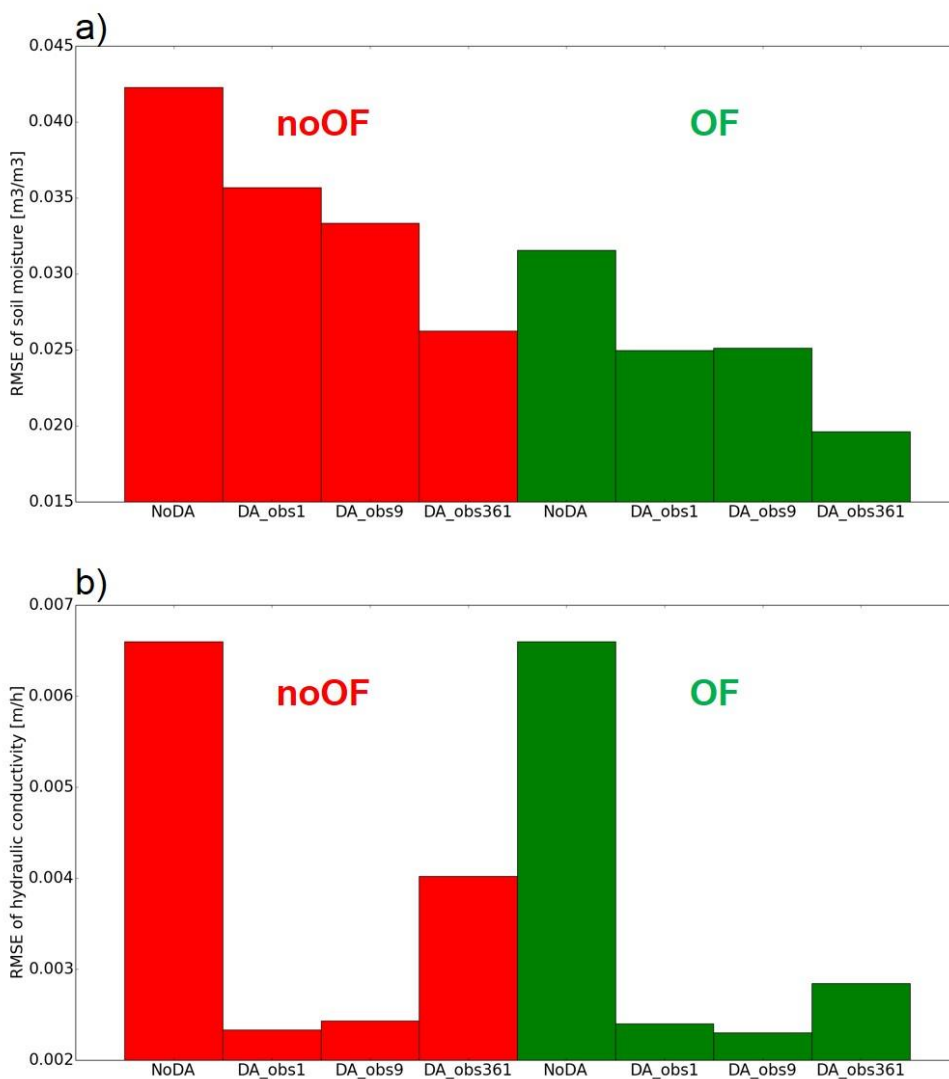
988

989

990



991

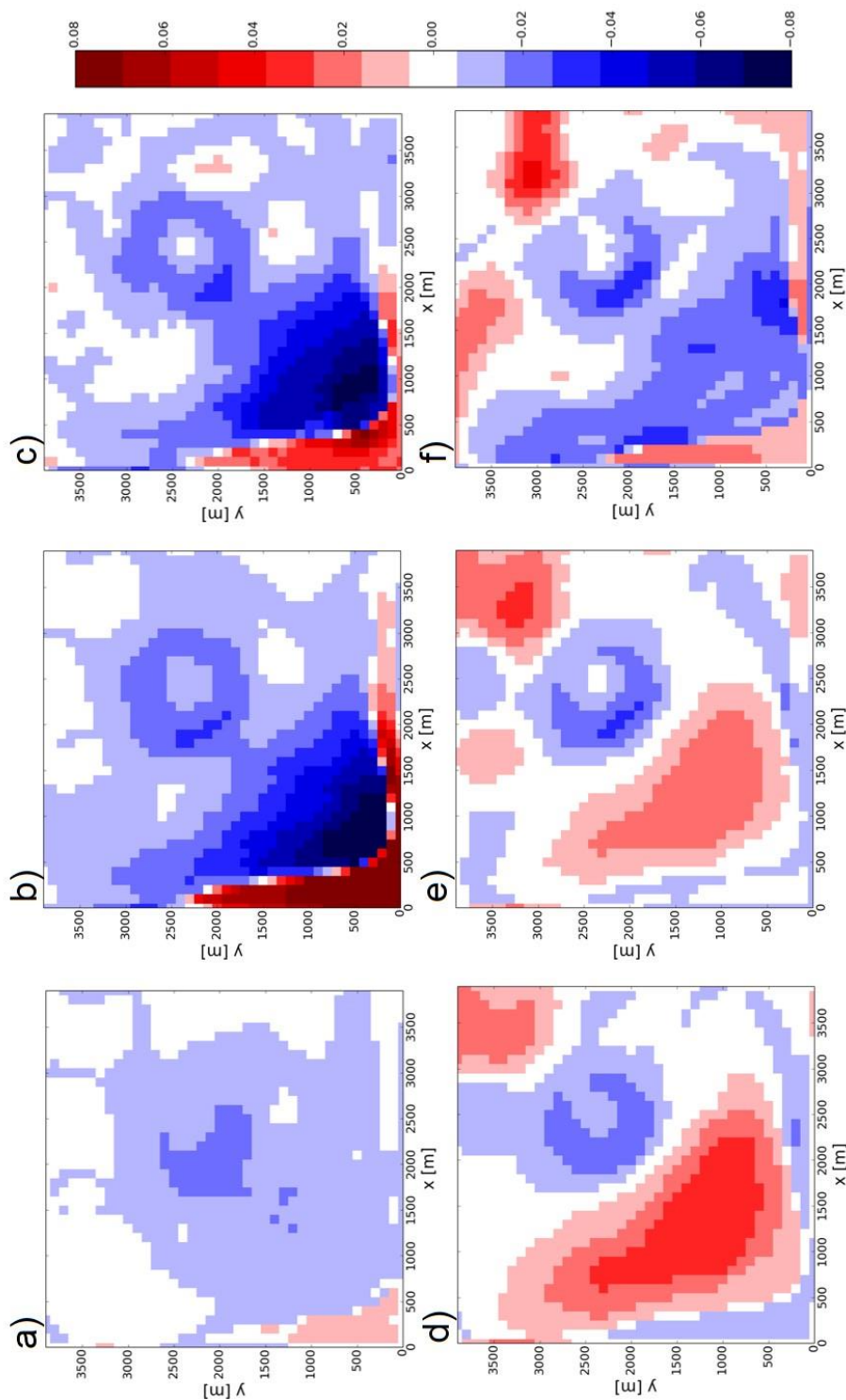


992

993 **Figure 8.** Time-mean RMSEs of the estimation of (a) soil moisture and (b) hydraulic conductivity. Red and

994 green bars are results of the noOF and OF configuration, respectively (see section 3.2.1 and Table 2).

995

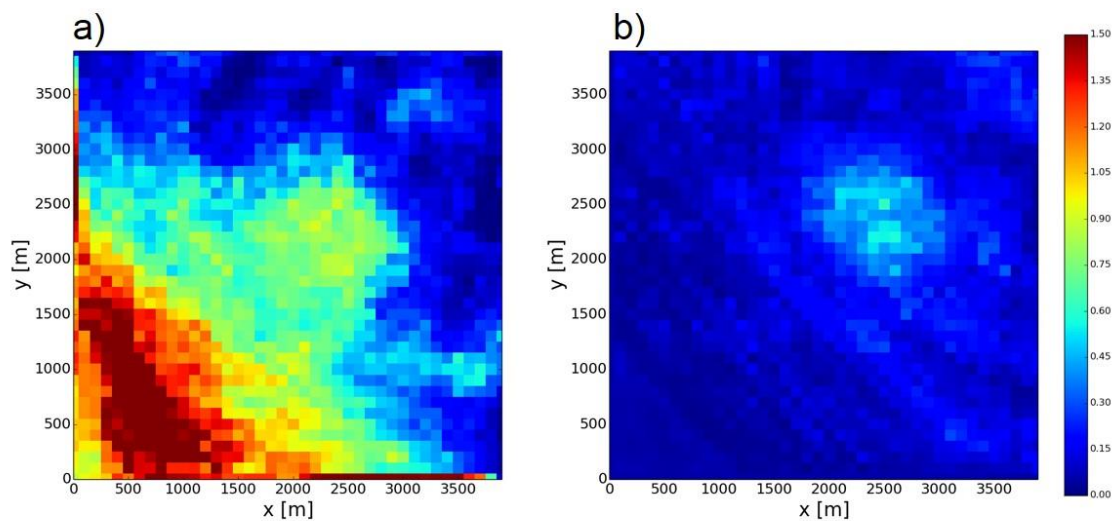


996  
997 **Figure 9.** Differences of time-mean soil moisture RMSEs between the DA experiments and the OF\_NoDA experiment. (a) OF\_DA\_obs1, (b) OF\_DA\_obs9 (c)  
998 OF\_DA\_obs361 (d) noOF\_DA\_obs1, (e) noOF\_DA\_obs9, (f) noOF\_DA\_obs361.





999



000

001

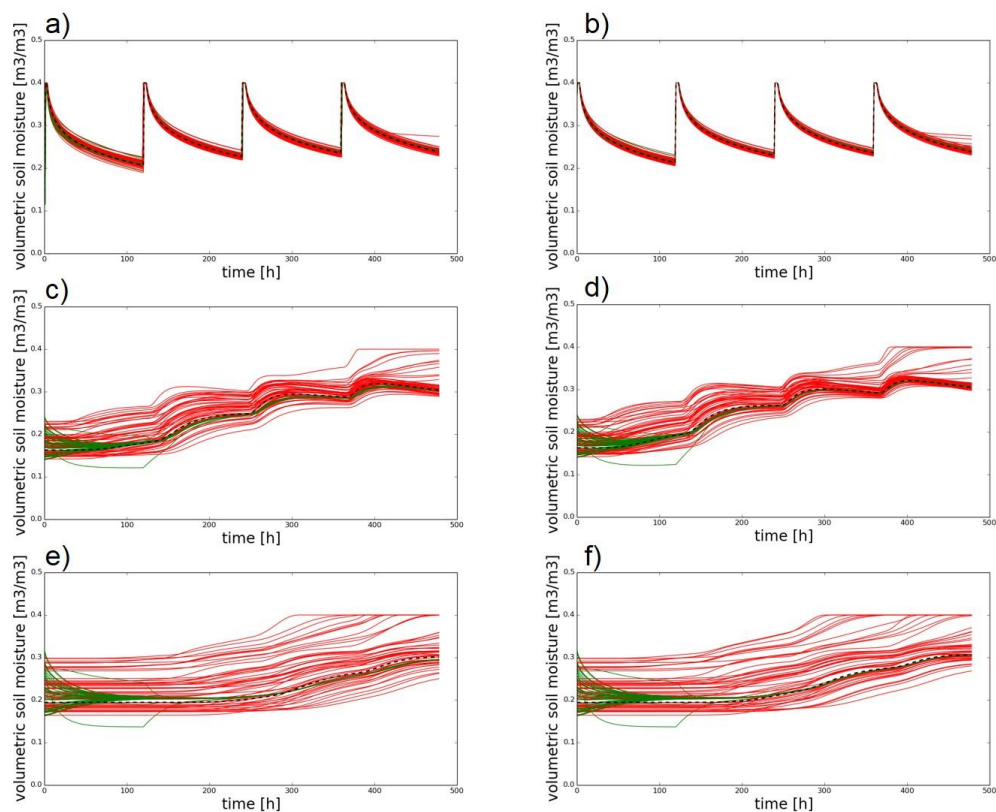
**Figure 10.** The Kullback-Leibler divergence of ensemble members generated by the (a) OF\_NoDA and (b) noOF\_NoDA experiments at  $t = 4$  [h].

002

003

004

005



006

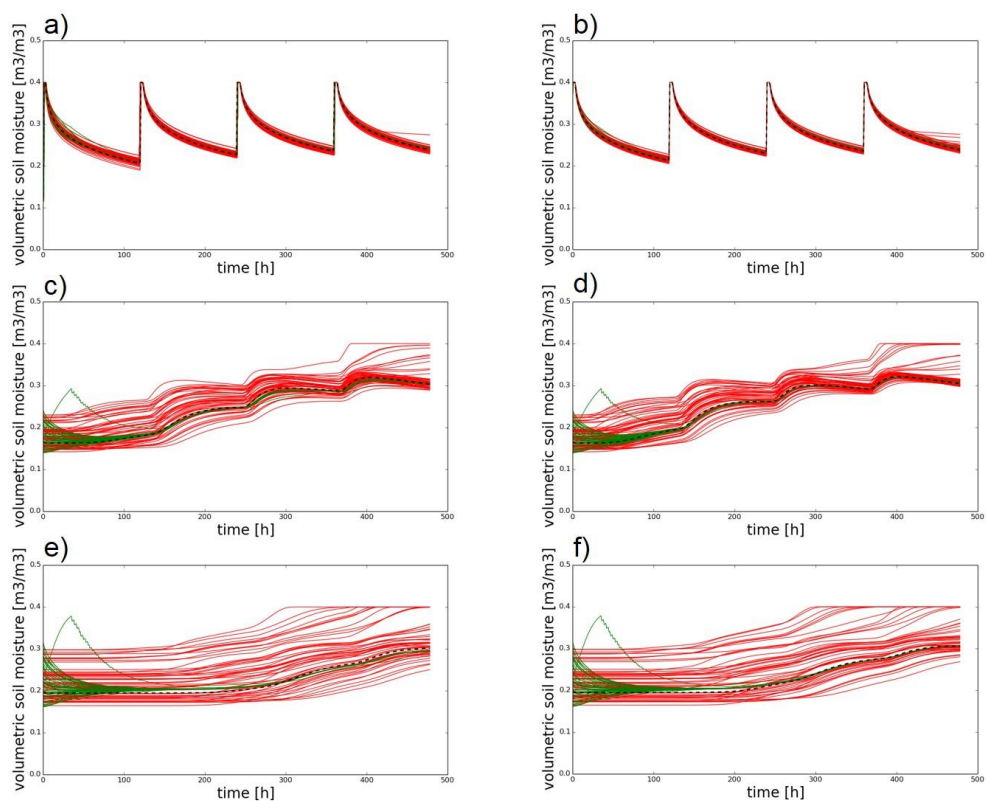
007 **Figure S1.** Time series of volumetric soil moisture simulated by the synthetic reference run (black dashed

008 line), the NoDA experiment (red lines), and the DA experiment (green lines) in the LOW\_K-UP\_O experiment

009 at a)  $x=1500\text{m}$ ,  $z=0.05\text{m}$ ; (b)  $x=2500\text{m}$ ,  $z=0.05\text{m}$ ; (c)  $x=1500\text{m}$ ,  $z=1.0\text{m}$ ; (d)  $x=2500\text{m}$ ,  $z=1.0\text{m}$ ; (e)  $x=1500\text{m}$ ,

010  $z=1.5\text{m}$ ; (f)  $x=2500\text{m}$ ,  $z=1.5\text{m}$ . In the DA experiment, initial guesses are used for this figure.

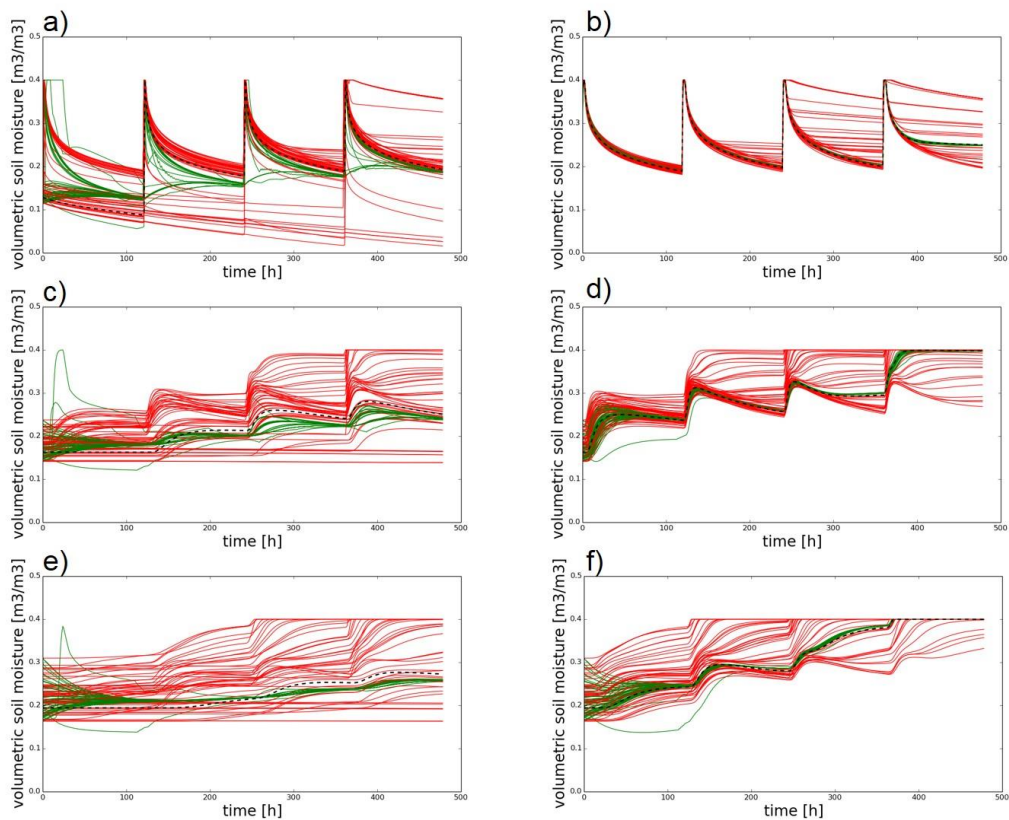
011



012

013 **Figure S2.** Same as Figure S1 but for the LOW\_K-DOWN\_O experiment.

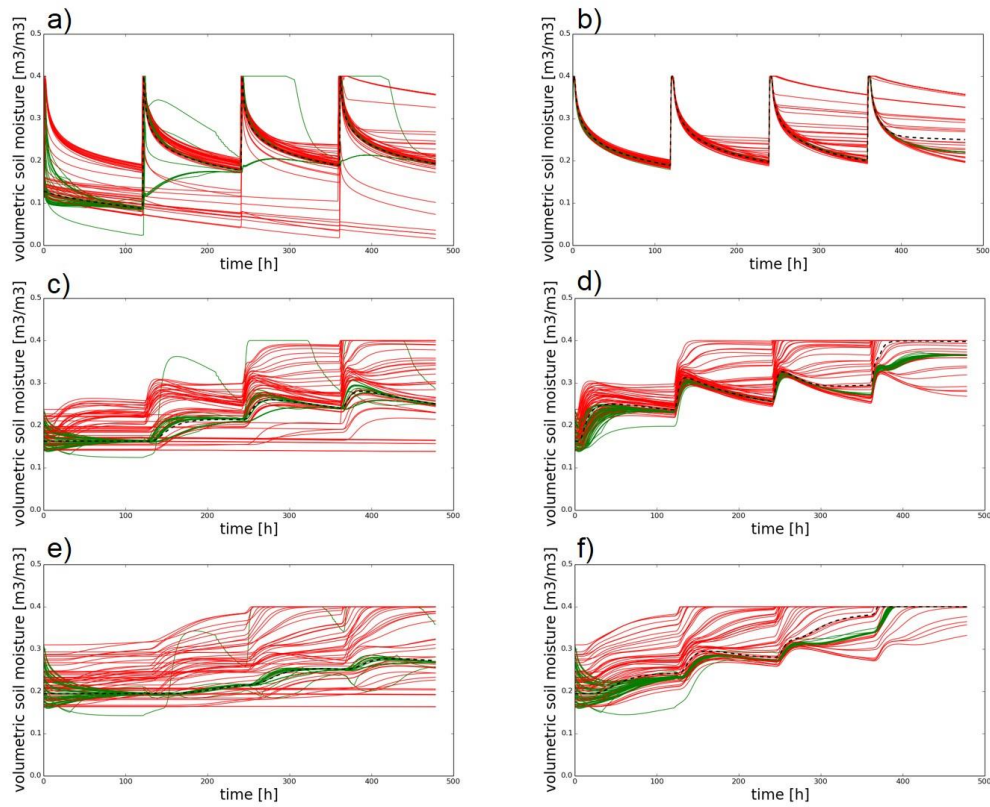
014



015

016 **Figure S3.** Same as Figure S1 but for the HIGH\_K-UP\_O experiment.

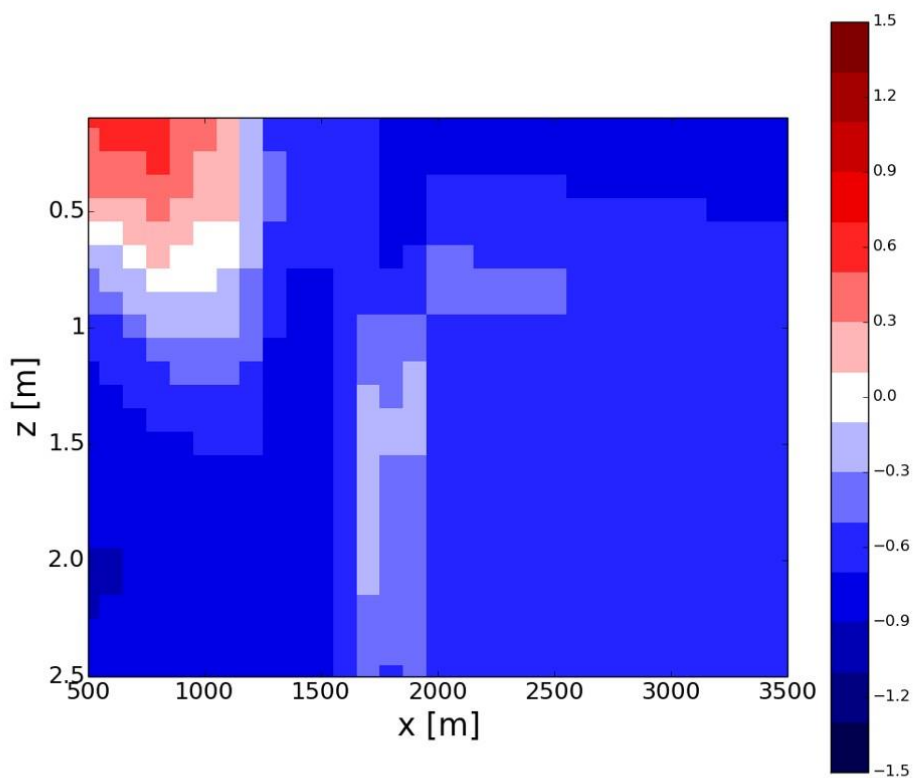
017



018

019 **Figure S4.** Same as Figure S1 but for the HIGH\_K-DOWN\_O experiment.

020



021

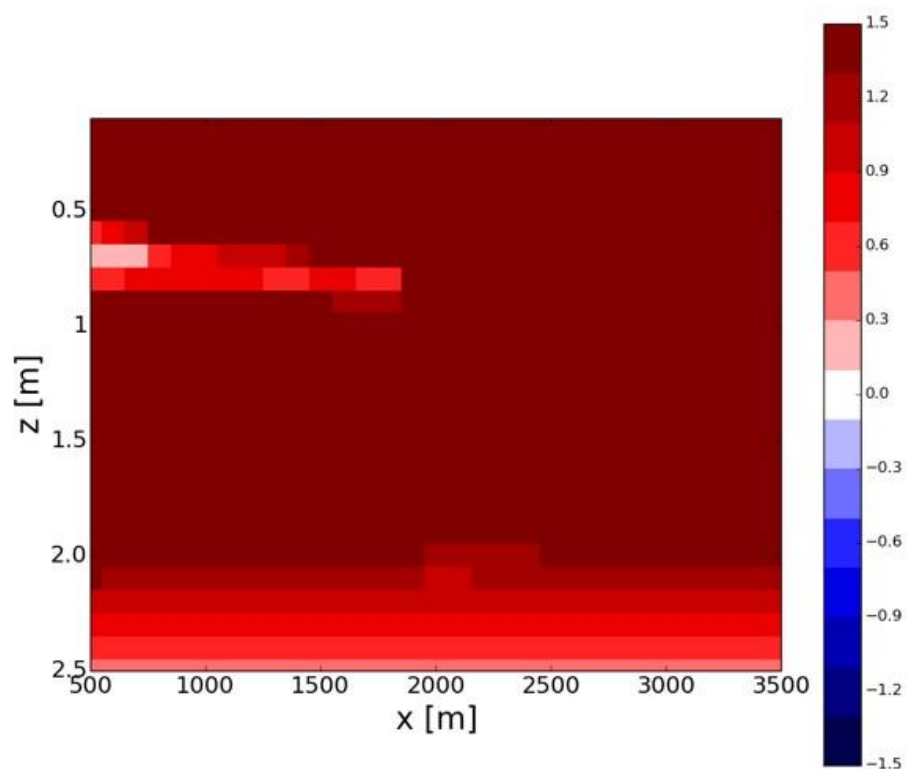
022 **Figure S5.** The improvement rates of the HIGH\_K-DOWN\_O experiment without a parameter optimization.

023

024



025

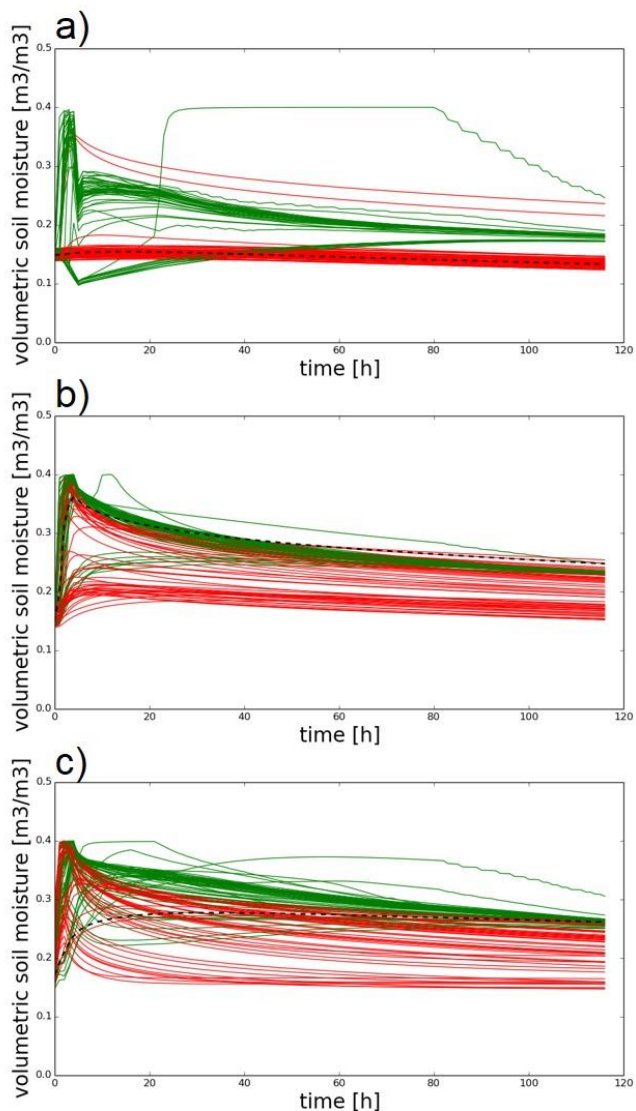


026

027 **Figure S6.** The improvement rates of the LOW\_K-DOWN\_O experiment where the topography-driven

028 surface flow is neglected in ParFlow.

029



030

031 **Figure S7.** Time series of volumetric soil moisture simulated by the synthetic reference run (black dashed

032 line), the OF\_NoDA experiment (red lines), and the OF\_DA\_obs361 experiment (green lines) at a)  $x=200\text{m}$ ,

033  $y=200\text{m}$ ,  $z=0.15\text{m}$ ; b)  $x=1200\text{m}$ ,  $y=1200\text{m}$ ,  $z=0.15\text{m}$ ; c)  $x=2200\text{m}$ ,  $y=2200\text{m}$ ,  $z=0.15\text{m}$ .

034